

Full-scatter vector field analysis of an overmoded and periodically-loaded cylindrical structure for the transportation of THz radiation

Adham Naji^{1,*}, Pawan Kumar Gupta¹, and Gennady Stupakov²

¹*Santa Clara University, Santa Clara, California, 95053*

²*SLAC National Accelerator Laboratory, Stanford, California, 94025*

(Dated: June 11, 2025)

The full-scatter vector field analysis of a highly overmoded and periodically loaded cylindrical waveguiding structure (or “iris line”) is presented. This type of structure is promising for the transportation of diffraction-prone short THz radiation pulses over hundreds of meters. The analysis uses vector fields, superseding scalar field descriptions, to account for polarization effects and ohmic loss on practical conductive screens. Its results are quite general, as it only assumes a paraxial incidence with slowly-varying envelope (parabolic wave equation) along the axis of the structure. It removes the traditional assumption of very thin screens, allowing for the study of thicker screens in the high-frequency limit, while hosting hundreds of modes and formulating the problem efficiently by scattering matrices whose coefficients are found analytically. The theory expands previously established methods, including Vainstein’s limit and the forward-scatter approximation, and validates them (as they become special cases with respect to it). It also facilitates accurate visualization of the transient regime at the entrance of the structure, and how it evolves to reach steady state.

I. INTRODUCTION

Practical overmoded structures that can guide high-frequency electromagnetic waves tend to be challenging to model, as they typically belong to a regime of analysis that lies between the limit of single-moded guided propagation and the limit of heavily diffractive propagation. The first limit assumes a relatively low frequency, as in traditional microwave waveguides or corrugated structures that offer phase velocity control (slow-wave ring-loaded structures in radiofrequency (rf) charged particle accelerators, for example). In this limit, one dominant mode is typically assumed, at least in some regions of the structure, and the analysis usually uses vector fields to account for polarization and conductive surface effects [1–10]. The second limit, on the other hand, tends to be concerned with thin edges and geometries, often with absorptive surface material, at higher frequencies. It typically uses scalar fields to describe diffraction effects, which can be well approximated asymptotically in some scenarios [1–9]. As boundary-value problems, we often analyze waveguiding structures spectrally (using a linear combination of the eigenmodes of the Helmholtz operator) or using integral equations (e.g. Green functions, factorization, or Wiener-Hopf techniques) [1–9, 11, 12].

When faced with a structure whose geometric features are oversized compared to the wavelength, λ , implying multi-mode (overmoded) operation, and made out of conductive material of finite thickness, $\delta \geq \lambda$, the required vector field analysis becomes more difficult. Standard numerical techniques, such as finite-element methods, may also become impractical due to the relatively large size of the structure compared to λ , forcing us to seek an analytical framework, not only to obtain a better insight into

the wave physics of the structure, but also to speed up field computations. Such a situation has been encountered during a study at the SLAC National Accelerator Laboratory, Stanford University, to transport a short THz pulse, in the 3–15 THz range, over hundreds of meters for use in pump-probe experiments (with a similar consideration at the European X-ray Free-Electron Laser, European XFEL, in Germany) [13–18]. One of the candidate solutions to transport the THz radiation without incurring too much loss to diffraction is the highly overmoded and periodically loaded cylindrical waveguide (or iris line) shown in Figure 1, [13–15]. When the screens are relatively thin, diffraction loss tends to be the dominant power loss mechanism during transportation [13–15]. Note that, for such oversized structures and short THz pulse applications, any part of the wave energy that is diffracted or scattered from the axial transportation direction (along z in Figure 1) into the shadow regions between the screens is considered lost. This allows one to model the conductive closed-chamber structure also as an open structure ($r_0 \rightarrow \infty$), or a closed one with an absorptive chamber and screen side-walls [14, 15].

Theoretical techniques, such as the eigen analysis based on mode matching [14] and the forward-scatter field analysis [15], were recently developed to take into account realistic screens with finite values of δ and to investigate the effects of ohmic loss. The former method solves an infinitely long structure for its steady-state eigenmodes, while the latter formulates each periodic section (cell) as a scattering problem, allowing flexibility in the analysis/design of finite length systems, while also boosting computational efficiency. The latter method, however, makes the assumption that the fields in each cell are scattered in the forward ($+z$) direction only, with no backward-traveling reflections [15]. Although this assumption is reasonable at the high-frequency limit, its main advantage is in reducing the complexity of the resulting equations so that we can readily extract the field

* anaji@scu.edu;

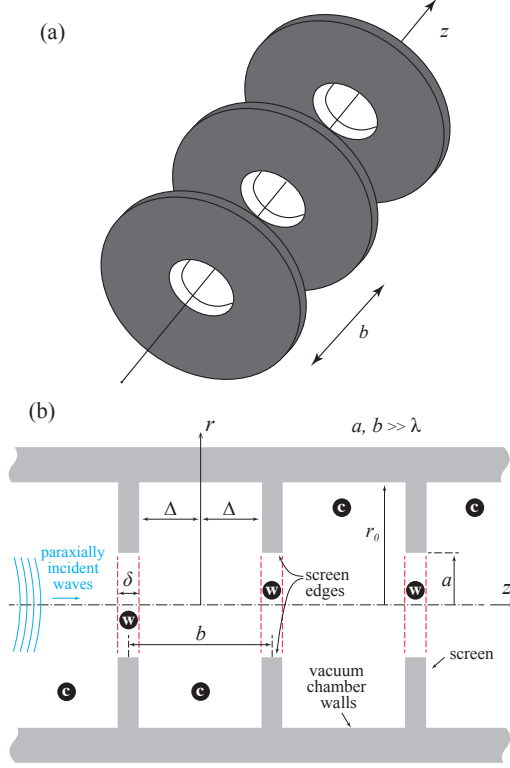


FIG. 1. A sketch showing the geometry of the iris line and the definition of key dimensions: (a) a three-dimensional sketch of the structure, without the enclosing vacuum chamber, (b) a cross-section, including the vacuum chamber. We separate the problem domain into two types of regions (subdomains): we call the regions with narrower radius ($r \leq a$) “waveguide” regions (indicated by a circle with the letter w in the figure), whereas regions with larger radius ($r \leq r_0$) are “cavity” regions (indicated by a circle with the letter c in the figure). The red dashed lines in the figure represent the planes for the “step-in” discontinuities (when traveling from a cavity to a waveguide region) and the “step-out” discontinuities (when traveling from a waveguide to a cavity region).

coefficients using mode orthogonality properties. A more rigorous analysis, however, will include a full-scatter formulation, where reflections are included and the coefficients of the spectral (modal) expansions of the fields are analytically produced. Conducting such an analysis will not only provide the most accurate results, but will also validate our usage of the forward-scattering approximation. To tackle the complexity of the full-scatter problem, we develop a special field formulation with the help of Lorentz’s reciprocity theorem, a theorem by Schelkunoff for source equivalence in scattering theory, and the field uniqueness theorem [1, 4, 7, 19–21]. To the best of our knowledge, this full-scatter spectral (modal) analysis has not been reported before.

The paper is organized as follows. In Section II we present the theoretical formulation of the problem in terms of full-scatter fields and obtain the analytical solutions for the field coefficients. Section III then discusses

the implementation of the theory using numerical examples, discusses the observed trends in ohmic and diffraction loss, as a function of δ , and demonstrates the agreement of the theory with previously established approximations and limits. The paper concludes in Section IV. Throughout the paper, we assume a time-harmonic dependence of the form $e^{-i\omega t}$, where ω is the angular frequency, t is time, and $i \equiv \sqrt{-1}$.

II. ANALYTICAL FORMULATION

A. Preliminary discussion

The transverse electric (TE) and transverse magnetic (TM) mode expansions in the waveguide and cavity regions were derived in [15] for the forward-traveling fields. We can extend these fields to include backward-traveling reflections by replacing the wavenumber $k \rightarrow -k$ in the same field derivation steps developed in [15]. Aside from the change in phase-propagation sign, the backward-traveling field expressions will have the same magnitude coefficients as those for the forward-traveling fields, except for the transverse magnetic (H_r, H_ϕ) and longitudinal electric (E_z) components, which will have the same magnitude but opposite sign compared to the forward-travel case. We adopt a notation where the superscripts “w”, “c” and “in” denote a waveguide-region field, a cavity-region field and an incident-mode field, respectively, and A_n^\pm or B_n^\pm denote the coefficients of the n th TE or TM mode, respectively. The \pm sign in the superscript indicates forward (+ z) or backward (− z) travel direction. The total field expressions are given by

$$E_{r,TE}^{\pm,w} = \sum_{n=1}^{\infty} \frac{A_n^\pm a}{\nu_{1n}' r} J_1(\nu_{1n}' \frac{r}{a}) \cos \phi \zeta_{TE} \quad (1)$$

$$E_{\phi,TE}^{\pm,w} = - \sum_{n=1}^{\infty} A_n^\pm J_1'(\nu_{1n}' \frac{r}{a}) \sin \phi \zeta_{TE} \quad (2)$$

$$E_{z,TE}^{\pm,w} = 0 \quad (3)$$

$$H_{r,TE}^{\pm,w} = \mp \sum_{n=1}^{\infty} \frac{A_n^\pm}{Z_0} \left(\frac{\nu_{1n}'^2}{2k^2 a^2} - 1 \right) J_1(\nu_{1n}' \frac{r}{a}) \sin \phi \zeta_{TE} \quad (4)$$

$$H_{\phi,TE}^{\pm,w} = \mp \sum_{n=1}^{\infty} \frac{A_n^\pm a}{Z_0 r \nu_{1n}'} \left(\frac{\nu_{1n}'^2}{2k^2 a^2} - 1 \right) J_1(\nu_{1n}' \frac{r}{a}) \cos \phi \zeta_{TE} \quad (5)$$

$$H_{z,TE}^{\pm,w} = - \sum_{n=1}^{\infty} \frac{i A_n^\pm \nu_{1n}'}{Z_0 k a} J_1(\nu_{1n}' \frac{r}{a}) \sin \phi \zeta_{TE} \quad (6)$$

$$E_{r,TM,n}^{\pm,w} = - \sum_{n=1}^{\infty} B_n^\pm J_1' \left(\nu_{1n} \frac{r}{a} \right) \cos \phi \zeta_{TM} \quad (7)$$

$$E_{\phi,TM,n}^{\pm,w} = \sum_{n=1}^{\infty} \frac{B_n^\pm a}{\nu_{1n} r} J_1 \left(\nu_{1n} \frac{r}{a} \right) \sin \phi \zeta_{TM} \quad (8)$$

$$E_{z,\text{TM},n}^{\pm,w} = \pm \sum_{n=1}^{\infty} \frac{iB_n^{\pm}\nu_{1n}}{ak} J_1\left(\nu_{1n}\frac{r}{a}\right) \cos\phi \zeta_{\text{TM}} \quad (9)$$

$$H_{r,\text{TM},n}^{\pm,w} = \mp \sum_{n=1}^{\infty} \frac{B_n^{\pm}a}{Z_0\nu_{1n}r} \left(\frac{\nu_{1n}^2}{2a^2k^2} + 1\right) J_1\left(\nu_{1n}\frac{r}{a}\right) \sin\phi \zeta_{\text{TM}} \quad (10)$$

$$H_{\phi,\text{TM},n}^{\pm,w} = \mp \sum_{n=1}^{\infty} \frac{B_n^{\pm}}{Z_0} \left(1 + \frac{\nu_{1n}^2}{2a^2k^2}\right) J_1'\left(\nu_{1n}\frac{r}{a}\right) \cos\phi \zeta_{\text{TM}} \quad (11)$$

$$H_{z,\text{TM},n}^{\pm,w} = 0 \quad (12)$$

where $\zeta_{\text{TE}} = e^{\pm(-iz\frac{\nu_{1n}^2}{2ka^2} + ikz)}$, $\zeta_{\text{TM}} = e^{\pm(-iz\frac{\nu_{1n}^2}{2ka^2} + ikz)}$, ϕ is the azimuthal angle in cylindrical coordinates, $Z_0 = 120\pi$ is the impedance of free space, J_1 denotes Bessel's function of the first kind and 1st-order, J_1' is its derivative with respect to its argument, ν_{1n} is the n th zero of J_1 , ν_{1n}' is the n th zero of J_1' , and the structure dimensions (a, b, r_0, δ) are defined in Figure 1.

The useful symmetric properties of the field equations (1)–(12) can be made clear during derivations by using a notation where we isolate the terms in front of each coefficient (A_n^{\pm} or B_n^{\pm}) as normalized expression for each mode. We denote these normalized expressions by a hat overscript. For example, in (1) we can define $\hat{E}_{r,\text{TE},n}^{+,w} \equiv \frac{a}{\nu_{1n}'r} J_1(\nu_{1n}'\frac{r}{a}) \cos\phi \zeta_{\text{TE}}$, and therefore the n th mode can be written as $E_{r,\text{TE},n}^{\pm,w} = A_n^{\pm} \hat{E}_{r,\text{TE},n}^{+,w}$, and so forth. Using this notation, (1)–(12) can be rewritten in a reduced form at $z = 0$ as

$$E_{r,\text{TE},n}^{\pm,w} = A_n^{\pm} \hat{E}_{r,\text{TE},n}^{+,w}, E_{r,\text{TM},n}^{\pm,w} = B_n^{\pm} \hat{E}_{r,\text{TM},n}^{+,w} \quad (13)$$

$$E_{\phi,\text{TE},n}^{\pm,w} = A_n^{\pm} \hat{E}_{\phi,\text{TE},n}^{+,w}, E_{\phi,\text{TM},n}^{\pm,w} = B_n^{\pm} \hat{E}_{\phi,\text{TM},n}^{+,w} \quad (14)$$

$$E_{z,\text{TE},n}^{\pm,w} = 0, E_{z,\text{TM},n}^{\pm,w} = \pm B_n^{\pm} \hat{E}_{z,\text{TM},n}^{+,w} \quad (15)$$

$$H_{r,\text{TE},n}^{\pm,w} = \pm A_n^{\pm} \hat{H}_{r,\text{TE},n}^{+,w}, H_{r,\text{TM},n}^{\pm,w} = \pm B_n^{\pm} \hat{H}_{r,\text{TM},n}^{+,w} \quad (16)$$

$$H_{\phi,\text{TE},n}^{\pm,w} = \pm A_n^{\pm} \hat{H}_{\phi,\text{TE},n}^{+,w}, H_{\phi,\text{TM},n}^{\pm,w} = \pm B_n^{\pm} \hat{H}_{\phi,\text{TM},n}^{+,w} \quad (17)$$

$$H_{z,\text{TE},n}^{\pm,w} = A_n^{\pm} \hat{H}_{z,\text{TE},n}^{+,w}, H_{z,\text{TM},n}^{\pm,w} = 0 \quad (18)$$

Note that the same equations are obtained for the cavity sections, if we replace the radius $a \rightarrow r_0$ and the superscript $w \rightarrow c$. For example, $E_{\phi,\text{TE},n}^{\pm,w}$ becomes $E_{\phi,\text{TE},n}^{\pm,c}$, and so forth.

Conducting a spectral (modal) analysis of the structure typically relies on expanding the locally scattered (or diffracted) field analytically in each region of the structure and matching such expansions at the discontinuity boundaries. This has been performed previously [15], where a single mode that is paraxially incident from the left side ($z < 0$) upon a discontinuity (step-in or step-out) positioned at $z = 0$ is matched to the modal expansion of field on the right side ($z > 0$). This method assumes no backward-traveling reflections (forward-scatter is considered dominant). The summation of one side of the equation is then reduced to one term with the help of mode orthogonality properties, allowing us to find the analyti-

cal expressions for the coefficients (A_n^{\pm}, B_n^{\pm}). The problem, however, becomes much more difficult when we try to derive the (A_n^{\pm}, B_n^{\pm}) coefficients in a full-scattered field analysis. The different mode summations with different radii in the Bessel function arguments will then exist on each side of the equation, rendering the usual orthogonality properties insufficient by themselves to reduce the problem. Traditional treatments seen in the literature often match modal expansions in uniform waveguides that have the same cross section on the left and right sides of a source region (singularity), or match them across discontinuous cross sections that assume only one (dominant) mode on one side, [1, 4, 7, 10]. In these cases, the analysis is easier and the modal sums are typically reduced using orthogonality integrals or a simple formulation of Lorentz's reciprocity theorem (discussed below). However, if a discontinuity has a cross-section change and many permissible modes are being scattered, literature treatments typically leave the result in terms of a sum of modes, without analytically finding the coefficients of these modes in explicit form. Alternative formulations, using variational, integral, or numerical techniques (e.g. [1, 3, 4]) are sometimes used in place of spectral analysis for such discontinuities.

In this Section, however, we show that one way of circumventing this difficulty is: (1) by carefully choosing an appropriate setup for the second field term ($\mathbf{E}_2, \mathbf{H}_2$) in Lorentz's reciprocity theorem, even when reflections are present and the cross-section is not uniform; (2) by utilizing a theorem by Schelkunoff for scattered field source equivalence, which allows us to decouple the different radii on each side of the discontinuity when applying orthogonality integrals; and (3) by utilizing uniqueness theorem for the field in a region with known source terms at the boundaries. To the best of our knowledge, the full analytical results derived in this paper, which are applicable to a general class of overmoded and periodically-loaded cylindrical guiding structures, have not been reported before in the literature.

Schelkunoff's theorem [4, 19], which originates from one of Schelkunoff's field scattering theorems (see Theorem no. 3 for electromagnetic waves in [19]), allows us to model a discontinuity by an equivalent current density sources (\mathbf{J}, \mathbf{M} , or both). With reference to Figure 2, we can obtain the fields at the LHS and RHS of the discontinuity, due to the original source by

$$(\mathbf{E}, \mathbf{H})_{z<0} = (\mathbf{E}_0, \mathbf{H}_0) + (\tilde{\mathbf{E}}^-, \tilde{\mathbf{H}}^-) \quad (19)$$

$$(\mathbf{E}, \mathbf{H})_{z>0} = (\tilde{\mathbf{E}}^+, \tilde{\mathbf{H}}^+), \quad (20)$$

where the $(\mathbf{E}_0, \mathbf{H}_0)$ is the field found when the $z > 0$ region is filled with a perfect electric conductor (PEC), and the scattered fields $(\tilde{\mathbf{E}}^{\pm}, \tilde{\mathbf{H}}^{\pm})$, denoted by a tilde symbol in the overscript, are the forward/backward-traveling fields generated by an equivalent current source at $z = 0$, when the PEC is present; namely,

$$\mathbf{J}(x, y, z) = \hat{n} \times \mathbf{H}_0(x, y, 0) \delta(z), \quad (21)$$

where $\delta(z)$ is the Dirac delta function in z . Thus, the need to match the field expansions in the $z > 0$ and $z < 0$ regions directly is removed by applying a singularity (current sources) at the interface.

In using this formalism, we have implicitly utilized uniqueness theorem [1, 21], which allows us to get a unique solution to the coupled Helmholtz wave equation or Maxwell equations for the fields in the volume, if we have a complete description of either \mathbf{J} , \mathbf{M} , or both source terms on the entirety of the enclosing surface walls. The choice of \mathbf{J} is therefore sufficient and convenient in the presence of the PEC ($z > 0$) and due to the conductive wall and aperture of the original problem in Figure 2. A discussion is given in Appendix A, which includes our proof of Schelkunoff's theorem and its application steps.

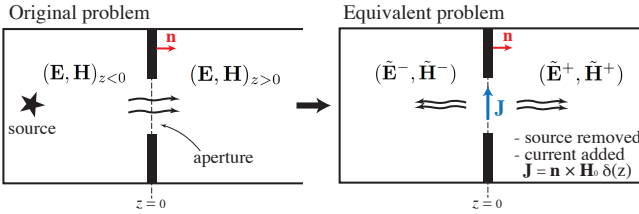


FIG. 2. A sketch demonstrating Schelkunoff's theorem. The original problem has a source and a field that fills the structure, passing through the aperture (opened in a conductive diaphragm, as indicated by the thick black lines). This original problem is replaced by an equivalent problem, whereby the original source is removed and an equivalent current source $\mathbf{J} = \hat{n} \times \mathbf{H}_0 \delta(z)$ is placed in the aperture's plane. The equivalent current density \mathbf{J} will produce scattered fields $(\tilde{\mathbf{E}}^-, \tilde{\mathbf{H}}^-)$ to the left, and $(\tilde{\mathbf{E}}^+, \tilde{\mathbf{H}}^+)$ to the right.

The general form of Lorentz's reciprocity theorem [1, 4] can be formulated by assuming two sets of electric and magnetic current density sources, $(\mathbf{J}_1, \mathbf{M}_1)$ and $(\mathbf{J}_2, \mathbf{M}_2)$, that generate two sets of corresponding fields $(\mathbf{E}_1, \mathbf{H}_1)$ and $(\mathbf{E}_2, \mathbf{H}_2)$, in a volume V enclosed by a Surface S . Divergence theorem and Maxwell's curl equations, $\nabla \times \mathbf{E} = i\omega\mu\mathbf{B} - \mathbf{M}$ and $\nabla \times \mathbf{H} = -i\omega\epsilon\mathbf{E} + \mathbf{J}$, are then combined to yield Lorentz's reciprocity theorem in integral form as

$$\oint_S (\mathbf{E}_2 \times \mathbf{H}_1 - \mathbf{E}_1 \times \mathbf{H}_2) \cdot d\mathbf{s} = \int_V (\mathbf{E}_1 \cdot \mathbf{J}_2 - \mathbf{H}_1 \cdot \mathbf{M}_2 - \mathbf{E}_2 \cdot \mathbf{J}_1 + \mathbf{H}_2 \cdot \mathbf{M}_1) dV \quad (22)$$

The usefulness of this tool stems from our ability to arbitrarily choose the $(\mathbf{E}_1, \mathbf{H}_1)$ or $(\mathbf{E}_2, \mathbf{H}_2)$ freely, as long as they satisfy Maxwell's equations. Most traditional treatments (e.g. see [1, 4, 7]) tend to analyze simpler scenarios with the first field set $(\mathbf{E}_1, \mathbf{H}_1)$ assumed to be the field expansion in a desired region, while the second field $(\mathbf{E}_2, \mathbf{H}_2)$ is only a single normalized mode from the modes in the full expansion, chosen to be traveling in the backward or forward direction, to obtain

the forward (A_n^+, B_n^+) or backward expansion coefficients (A_n^-, B_n^-) , respectively [1]. This traditional choice, however, will not be valid in the full-scatter analysis in a non-uniform structure, and we utilize a different choice for $(\mathbf{E}_2, \mathbf{H}_2)$, as shown below in Subsections II B–II D, where we find the analytical solutions for the four coefficients $(A_n^-, B_n^-, A_n^+, B_n^+)$ for TE or TM incidence on a step-in or step-out discontinuity. The total is a set of 16 equations.

Note that all of the fields written in the following sections for the full-scatter derivations are the transverse fields (e.g. $\mathbf{E} \equiv \mathbf{E}_\perp$), unless otherwise stated, and we can always choose $z = 0$ locally to be at the plane of the discontinuity under considerations (longitudinal phase evolution will be taken care of later through propagator matrices).

B. Analysis of TM incidence on a step-in discontinuity

Consider the full-scatter fields resulting from a single TM mode (index ℓ) that is incident upon a step-in discontinuity, as shown in Figure 3. Applying reciprocity theorem and Schelkunoff's theorem to this discontinuity, as demonstrated in Figure 4, we can write the transverse fields $(\mathbf{E}_1, \mathbf{H}_1)$ at the discontinuity plane ($z = 0$) in terms of the combined incident, reflected and transmitted fields. Specifically, the incident field $(\mathbf{E}_{\text{TM},\ell}^{\text{in},c}, \mathbf{H}_{\text{TM},\ell}^{\text{in},c})$ gives rise to the equivalent current source

$$\mathbf{J}_1 = +\hat{n} \times \mathbf{H}_0 = \hat{n} \times 2\mathbf{H}_{\text{TM},\ell}^{\text{in},c} = 2B_\ell^{\text{in}} \hat{n} \times \hat{\mathbf{H}}_{\text{TM},\ell}^{\text{in},c}, \quad (23)$$

where we have followed the same notation of reciprocity theorem, taking \mathbf{J}_1 as the current source equivalent for the discontinuity (aperture) and the first set of fields $(\mathbf{E}_1, \mathbf{H}_1)$ as the fields reflected or transmitted it.

The reflected fields $(\mathbf{E}_1 = \mathbf{E}_1^-, \mathbf{H}_1 = \mathbf{H}_1^-)$ in $z < 0$ and transmitted fields $(\mathbf{E}_1 = \mathbf{E}_1^+, \mathbf{H}_1 = \mathbf{H}_1^+)$ in $z > 0$, on the other hand, are given by

$$\begin{aligned} \mathbf{E}_1^- &= \sum_n \mathbf{E}_{\text{TM},n}^{-,c} + \sum_n \mathbf{E}_{\text{TE},n}^{-,c} \\ &= \sum_n B_n^- \hat{\mathbf{E}}_{\text{TM},n}^{+,c} + \sum_n A_n^- \hat{\mathbf{E}}_{\text{TE},n}^{+,c} = \sum_n D_n^- \hat{\mathbf{E}}_n^{+,c} \end{aligned} \quad (24)$$

$$\begin{aligned} \mathbf{H}_1^- &= \sum_n \mathbf{H}_{\text{TM},n}^{-,c} + \sum_n \mathbf{H}_{\text{TE},n}^{-,c} \\ &= -\sum_n B_n^- \hat{\mathbf{H}}_{\text{TM},n}^{+,c} - \sum_n A_n^- \hat{\mathbf{H}}_{\text{TE},n}^{+,c} = -\sum_n D_n^- \hat{\mathbf{H}}_n^{+,c} \end{aligned} \quad (25)$$

$$\begin{aligned} \mathbf{E}_1^+ &= \sum_n \mathbf{E}_{\text{TM},n}^{+,w} + \sum_n \mathbf{E}_{\text{TE},n}^{+,w} \\ &= \sum_n B_n^+ \hat{\mathbf{E}}_{\text{TM},n}^{+,w} + \sum_n A_n^+ \hat{\mathbf{E}}_{\text{TE},n}^{+,w} = \sum_n D_n^+ \hat{\mathbf{E}}_n^{+,w} \end{aligned} \quad (26)$$

$$\begin{aligned}
\mathbf{H}_1^+ &= \sum_n \mathbf{H}_{\text{TM},n}^{+,w} + \sum_n \mathbf{H}_{\text{TE},n}^{+,w} \\
&= - \sum_n B_n^+ \hat{\mathbf{H}}_{\text{TM},n}^{+,w} - \sum_n A_n^+ \hat{\mathbf{H}}_{\text{TE},n}^{+,w} = - \sum_n D_n^+ \hat{\mathbf{H}}_n^{+,w}
\end{aligned} \tag{27}$$

where we have made use of (13)–(18) to reduce all expressions in terms of the forward normalized fields (i.e. $\hat{\mathbf{E}}_n^+, \hat{\mathbf{H}}_n^+$) and, for brevity, used the notation of $\mathbf{E}_n, \mathbf{H}_n$ and D_n^\pm (without explicit TE or TM subscripts) to imply that both A_n and B_n (for TE and TM) are absorbed in the final indexed sum.

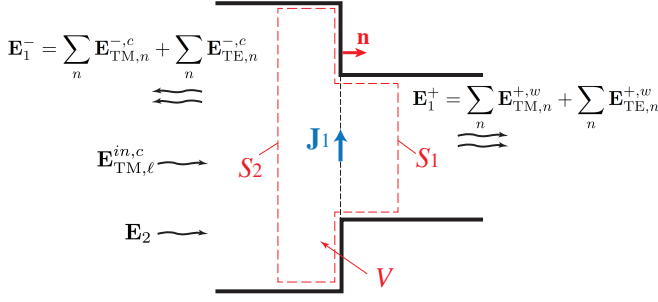


FIG. 3. An example of step-in discontinuity with a TM incidence. For clarity, only the E fields are explicitly shown in this figure. The integration surfaces on the right and left hand sides of the volume V are denoted by S_1 and S_2 , and are immediately adjacent to each side of the plane $z = 0$ (note that the figure is showing exaggerated distances between the surfaces S_1, S_2 and $z = 0$ for clarity). Here, a single mode is incident ($\mathbf{E}_{\text{TM},\ell}^{+,c}$), and a field is reflected back into the waveguide region (\mathbf{E}_1^-) and a field is transmitted onto the cavity region (\mathbf{E}_1^+), as given by (24) and (26). The reflected and transmitted fields can be in both TE and TM in general. Analogous geometries, fields and surfaces can be constructed for the step-out discontinuity and TE/TM incidences.

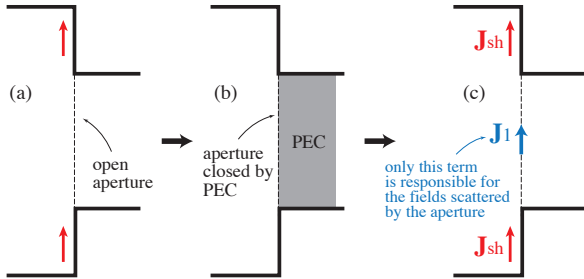


FIG. 4. When constructing the equivalent problem, by starting from the original problem (a), filling the aperture with a perfect electric conductor (PEC), and then replacing the aperture by an equivalent current \mathbf{J}_1 (c), is important to distinguish between the surface current \mathbf{J}_{sh} , due to the “shoulders” of the step-in structure, which will always be there, and the current \mathbf{J}_1 that models only the aperture. Only the latter is the source concerned for generating the scattered fields, ($\mathbf{E}_1^\pm, \mathbf{H}_1^\pm$), as in Schelkunoff’s theorem.

Given that the full-scatter fields on each side of the discontinuity are happening in regions of different radii,

a careful choice of the field \mathbf{E}_2 in reciprocity theorem will allow us to proceed to find all the reflection (A^-, B^-) and transmission (A^+, B^+) coefficients analytically. We do so by choosing one of the following *scenarios* for \mathbf{E}_2 (it is easy to deduce \mathbf{H}_2 from \mathbf{E}_2):

(1) To find B_m^- , take

$$\mathbf{E}_2 = \begin{cases} \hat{\mathbf{E}}_{\text{TM},m}^{+,c}, & z < 0 \\ \sum_p \alpha_{m,p}^+ \hat{\mathbf{E}}_p^{+,w}, & z > 0 \end{cases} \tag{28}$$

Here, E_2 is incident from the cavity region toward the right side, and $\alpha_{m,p}^+$ are some expansion coefficients for the mode in terms of waveguide modes.

(2) To find A_m^- , take

$$\mathbf{E}_2 = \begin{cases} \hat{\mathbf{E}}_{\text{TE},m}^{+,c}, & z < 0 \\ \sum_p \beta_{m,p}^+ \hat{\mathbf{E}}_p^{+,w}, & z > 0 \end{cases} \tag{29}$$

Here, E_2 is incident from cavity toward the right side, and $\beta_{m,p}^+$ are some expansion coefficients for the mode in terms of waveguide modes.

(3) To find B_m^+ , take

$$\mathbf{E}_2 = \begin{cases} \sum_p \gamma_{m,p}^- \hat{\mathbf{E}}_p^{-,c}, & z < 0 \\ \hat{\mathbf{E}}_{\text{TM},m}^{-,w}, & z > 0 \end{cases} \tag{30}$$

Here, E_2 is incident from the waveguide region toward the left side, and $\gamma_{m,p}^-$ are some expansion coefficients for the mode in terms of cavity modes.

(4) To find A_m^+ , take

$$\mathbf{E}_2 = \begin{cases} \sum_p \zeta_{m,p}^- \hat{\mathbf{E}}_p^{-,c}, & z < 0 \\ \hat{\mathbf{E}}_{\text{TE},m}^{-,w}, & z > 0 \end{cases} \tag{31}$$

Here, E_2 is incident from the waveguide region toward the left side, and $\zeta_{m,p}^-$ are some expansion coefficients for the mode in terms of cavity modes.

In the above expressions, \mathbf{E}_p denotes both TE and TM modes, for brevity. The expansion coefficients (such as $\zeta_{m,p}^-$, for example) will thus also include those for TE and TM modes. For example, one can write more explicitly $\sum_p \zeta_{m,p}^- \hat{\mathbf{E}}_p^{-,c}$ as $\sum_p B_{m,p}^- \hat{\mathbf{E}}_{\text{TM},p}^{-,c} + \sum_p A_{m,p}^- \hat{\mathbf{E}}_{\text{TE},p}^{-,c}$, and so forth. Note that we can derive the analytical expressions for $\alpha_{m,p}^+, \beta_{m,p}^+, \gamma_{m,p}^-$ and $\zeta_{m,p}^-$ explicitly in the above scenarios, but we do not actually need to, as we will see below. Bearing in mind that $\mathbf{J}_2 = 0$ and $\mathbf{M}_1 = \mathbf{M}_2 = 0$, reciprocity theorem (22) now becomes

$$\oint_S (\mathbf{E}_2 \times \mathbf{H}_1 - \mathbf{E}_1 \times \mathbf{H}_2) \cdot d\mathbf{s} = - \int_V \mathbf{E}_2 \cdot \mathbf{J}_1 dV \tag{32}$$

For each of the four scenarios above, we now use (24)–(27) and (32), to find all A_m^-, A_m^+, B_m^- and B_m^+ .

Consider *Scenario* (1) to find B_m^- , with (28), we find the LHS (surface integral) of (32), bearing in mind that $\oint_S \equiv \int_{S_1} + \int_{S_2}$ (see Figure 3 for the definition of surfaces S_1 and S_2), as

$$\begin{aligned}
\int_{S_2} (\mathbf{E}_2 \times \mathbf{H}_1 - \mathbf{E}_1 \times \mathbf{H}_2) \cdot d\mathbf{s} &= - \int_0^{2\pi} \int_0^{r_0} r dr d\phi \hat{z} \cdot \left[\hat{\mathbf{E}}_{\text{TM},m}^{+,c} \times \sum_n D_n^- \hat{\mathbf{H}}_n^{-,c} - \sum_n D_n^- \hat{\mathbf{H}}_n^{-,c} \times \hat{\mathbf{E}}_{\text{TM},m}^{+,c} \right] \\
&= - \sum_n D_n^- \left[\iint r dr d\phi \hat{z} \cdot \left(\hat{\mathbf{E}}_{\text{TM},m}^{+,c} \times \hat{\mathbf{H}}_n^{-,c} \delta_{mn} - \hat{\mathbf{H}}_n^{-,c} \times \hat{\mathbf{E}}_{\text{TM},m}^{+,c} \delta_{mn} \right) \right] \\
&= -\tilde{B}_m^- \left[\iint r dr d\phi \hat{z} \cdot \left(-\hat{\mathbf{E}}_{\text{TM},m}^{+,c} \times \hat{\mathbf{H}}_{\text{TM},m}^{+,c} - \hat{\mathbf{E}}_{\text{TM},m}^{+,c} \times \hat{\mathbf{H}}_{\text{TM},m}^{+,c} \right) \right] \\
&= +2\tilde{B}_m^- \underbrace{\iint r dr d\phi \hat{z} \cdot (\hat{\mathbf{E}}_{\text{TM},m}^{+,c} \times \hat{\mathbf{H}}_{\text{TM},m}^{+,c})}_{=2\hat{P}_{\text{TM},m}^c} = +4\tilde{B}_m^- \hat{P}_{\text{TM},m}^c \tag{33}
\end{aligned}$$

$$\begin{aligned}
\int_{S_1} (\mathbf{E}_2 \times \mathbf{H}_1 - \mathbf{E}_1 \times \mathbf{H}_2) \cdot d\mathbf{s} &= + \iint r dr d\phi \hat{z} \cdot \left[\sum_p \alpha_{m,p}^+ \hat{\mathbf{E}}_p^{+,w} \times \sum_n D_n^+ \hat{\mathbf{H}}_n^{+,w} - \sum_n D_n^+ \hat{\mathbf{E}}_n^{+,w} \times \sum_p \alpha_{m,p}^+ \hat{\mathbf{H}}_p^{+,w} \right] \\
&= \sum_{n,p} \alpha_{m,p}^+ D_n^+ \iint r dr d\phi \hat{z} \cdot \left(\hat{\mathbf{E}}_p^{+,w} \times \hat{\mathbf{H}}_n^{+,w} - \hat{\mathbf{E}}_n^{+,w} \times \hat{\mathbf{H}}_p^{+,w} \right) = 0 \\
\Rightarrow \int_{S_1} + \int_{S_2} &\equiv \oint_S (\mathbf{E}_2 \times \mathbf{H}_1 - \mathbf{E}_1 \times \mathbf{H}_2) \cdot d\mathbf{s} = 0 + 4\tilde{B}_m^- \hat{P}_{\text{TM},m}^c = 4\tilde{B}_m^- \hat{P}_{\text{TM},m}^c \tag{34}
\end{aligned}$$

where \tilde{B}_m^- denotes the coefficients of the TM mode scattered by the equivalent source \mathbf{J}_1 , and $\hat{P}_{\text{TM},m}^c$ denotes the complex power carried by the m th normalized TM mode from the cavity section side. The integrals on surfaces S_1 and S_2 will carry an opposite sign relative to each other, due to their surface normal vectors being along \hat{n} (shown in Figure 3) or opposite to it, respectively. Note that the appearance of the Kronecher delta function, δ_{mn} , is

a direct result of the orthogonality of cavity modes of different type (TE/TM) or same type but different index. The integration domain over the azimuthal angle, ϕ , are 0 to 2π radians, and over the radial direction, r , are 0 to r_0 . Throughout most of the integrals in this paper, the only limit that will change is the upper limit for the integral in r , depending on the region. It will therefore be the only limit explicitly displayed.

The volume integral in the RHS of (32) gives

$$\begin{aligned}
- \int_V dV \mathbf{E}_2 \cdot \mathbf{J}_1 &= - \iiint r dr d\phi dz \left[\hat{\mathbf{E}}_{\text{TM},m}^{+,c} \cdot \left(2\hat{z} \times \hat{\mathbf{H}}_{\text{TM},\ell}^{+,c} \right) B_\ell^{in} \delta(z) \right] \\
&= +2B_\ell^{in} \iint r dr d\phi \left(\hat{E}_{r\text{TM},m}^{+,c} \hat{H}_{\phi\text{TM},\ell}^{+,c} - \hat{E}_{\phi\text{TM},m}^{+,c} \hat{H}_{r\text{TM},\ell}^{+,c} \right) \\
&= +B_\ell^{in} \frac{2\pi}{Z_0} \left(1 + \frac{\nu_{1\ell}^2}{2k^2 r_0^2} \right) \int^a dr \left[r J_1' \left(\frac{\nu_{1m} r}{r_0} \right) J_1' \left(\frac{\nu_{1\ell} r}{r_0} \right) + \frac{r_0^2}{\nu_{1m} \nu_{1\ell} r} J_1 \left(\frac{\nu_{1m} r}{r_0} \right) J_1 \left(\frac{\nu_{1\ell} r}{r_0} \right) \right] \\
&= \frac{\pi B_\ell^{in}}{Z_0} \left(1 + \frac{\nu_{1\ell}^2}{2k^2 r_0^2} \right) \int^a dr r \left[J_0 \left(\frac{\nu_{1m} r}{r_0} \right) J_0 \left(\frac{\nu_{1\ell} r}{r_0} \right) + J_2 \left(\frac{\nu_{1m} r}{r_0} \right) J_2 \left(\frac{\nu_{1\ell} r}{r_0} \right) \right] = \frac{\pi B_\ell^{in}}{Z_0} \left(1 + \frac{\nu_{1\ell}^2}{2k^2 r_0^2} \right) \begin{cases} \Psi_1, & m = \ell \\ \Psi_2, & m \neq \ell \end{cases} \tag{35}
\end{aligned}$$

where

$$\Psi_1 = \frac{a^2}{2} \left[J_0^2 \left(\frac{\nu_{1\ell} a}{r_0} \right) + J_1^2 \left(\frac{\nu_{1\ell} a}{r_0} \right) + J_2^2 \left(\frac{\nu_{1\ell} a}{r_0} \right) - J_1 \left(\frac{\nu_{1\ell} a}{r_0} \right) J_3 \left(\frac{\nu_{1\ell} a}{r_0} \right) \right] \tag{36}$$

$$\Psi_2 = \frac{ar_0}{\nu_{1\ell}^2 - \nu_{1m}^2} \left\{ \nu_{1\ell} J_1 \left(\frac{\nu_{1\ell} a}{r_0} \right) \left[J_0 \left(\frac{\nu_{1m} a}{r_0} \right) - J_2 \left(\frac{\nu_{1m} a}{r_0} \right) \right] + \nu_{1m} J_1 \left(\frac{\nu_{1m} a}{r_0} \right) \left[J_2 \left(\frac{\nu_{1\ell} a}{r_0} \right) - J_0 \left(\frac{\nu_{1\ell} a}{r_0} \right) \right] \right\} \tag{37}$$

Equating (34) and (35) gives

$$\tilde{B}_m^- = \frac{\pi B_\ell^{in}}{4Z_0 \hat{P}_{\text{TM},m}^c} \left(1 + \frac{\nu_{1\ell}^2}{2k^2 r_0^2} \right) \begin{cases} \Psi_1, & m = \ell \\ \Psi_2, & m \neq \ell \end{cases} \tag{38}$$

Recall that this reflected field is only due to the equiv-

alent source \mathbf{J}_1 and we still need to add it to the \mathbf{H}_0 field (produced by the PEC aperture filling), which has

$B_0^- = B_\ell^{in} \delta_{m\ell}$ (same magnitude as the incident wave). Thus, we arrive at the reflection coefficient

$$B_m^- = B_0^- + \tilde{B}_m^- = B_\ell^{in} \delta_{m\ell} + \tilde{B}_m^- \quad (39)$$

$$= \begin{cases} B_\ell^{in} \left\{ -1 + \frac{\pi a^2 \left(1 + \frac{\nu_{1\ell}^2}{2k^2 r_0^2} \right)}{8Z_0 \hat{P}_{\text{TM},\ell}^c} \left[J_0^2 \left(\frac{\nu_{1\ell} a}{r_0} \right) + J_1^2 \left(\frac{\nu_{1\ell} a}{r_0} \right) + J_2^2 \left(\frac{\nu_{1\ell} a}{r_0} \right) - J_1 \left(\frac{\nu_{1\ell} a}{r_0} \right) J_3 \left(\frac{\nu_{1\ell} a}{r_0} \right) \right] \right\}, & m = \ell \\ \frac{\pi B_\ell^{in} a r_0 \left(1 + \frac{\nu_{1\ell}^2}{2k^2 r_0^2} \right)}{4Z_0 \hat{P}_{\text{TM},m}^c (\nu_{1\ell}^2 - \nu_{1m}^2)} \left\{ \nu_{1\ell} J_1 \left(\frac{\nu_{1\ell} a}{r_0} \right) \left[J_0 \left(\frac{\nu_{1m} a}{r_0} \right) - J_2 \left(\frac{\nu_{1m} a}{r_0} \right) \right] + \nu_{1m} J_1 \left(\frac{\nu_{1m} a}{r_0} \right) \left[J_2 \left(\frac{\nu_{1\ell} a}{r_0} \right) - J_0 \left(\frac{\nu_{1\ell} a}{r_0} \right) \right] \right\}, & m \neq \ell \end{cases} \quad (40)$$

We observe from (40) how the reflected mode whose index (m) is the same as the incident mode index (ℓ) will have a different expression compared to modes of different index ($m \neq \ell$). This is expected, since the coupling between the mode and its own reflected wave

(same index) will naturally differ from the coupling with others modes, due to the discontinuity.

Consider now *Scenario* (2), to find A_m^- , by taking \mathbf{E}_2 in (29) and applying (32) in a similar fashion as the first scenario. We find for the LHS and RHS of (32) as

$$\oint_S (\mathbf{E}_2 \times \mathbf{H}_1 - \mathbf{E}_1 \times \mathbf{H}_2) \cdot d\mathbf{s} = 0 + 4\tilde{A}_m^- \hat{P}_{\text{TE},m}^c = 4\tilde{A}_m^- \hat{P}_{\text{TE},m}^c \quad (41)$$

$$- \int_V dV \mathbf{E}_2 \cdot \mathbf{J}_1 = - \iiint^a r dr d\phi dz \left[\hat{\mathbf{E}}_{\text{TE},m}^{+,c} \cdot \left(2\hat{\mathbf{z}} \times \hat{\mathbf{H}}_{\text{TM},\ell}^{+,c} \right) B_\ell^{in} \delta(z) \right]$$

$$= +2B_\ell^{in} \iint^a r dr d\phi \left(\hat{E}_{r\text{TE},m}^{+,c} \hat{H}_{\phi\text{TM},\ell}^{+,c} - \hat{E}_{\phi\text{TE},m}^{+,c} \hat{H}_{r\text{TM},\ell}^{+,c} \right)$$

$$= -B_\ell^{in} \frac{2\pi}{Z_0} \left(1 + \frac{\nu_{1\ell}^2}{2k^2 r_0^2} \right) \int^a dr \left[\frac{r_0}{\nu_{1m}'} J_1 \left(\frac{\nu_{1m}' r}{r_0} \right) J_1' \left(\frac{\nu_{1\ell} r}{r_0} \right) + \frac{r_0}{\nu_{1\ell}} J_1' \left(\frac{\nu_{1m}' r}{r_0} \right) J_1 \left(\frac{\nu_{1\ell} r}{r_0} \right) \right]$$

$$= -B_\ell^{in} \frac{2\pi}{Z_0} \left(1 + \frac{\nu_{1\ell}^2}{2k^2 r_0^2} \right) \frac{r_0^2 J_1 \left(\frac{\nu_{1m}' a}{r_0} \right) J_1 \left(\frac{\nu_{1\ell} a}{r_0} \right)}{\nu_{1\ell} \nu_{1m}'}, \quad (42)$$

where $\hat{P}_{\text{TE},m}^c$ denotes the complex power carried by the m th normalized TE mode from the cavity section side.

Upon equating the (41) and (42), we obtain

$$\tilde{A}_m^- = - \frac{\pi B_\ell^{in}}{2Z_0 \hat{P}_{\text{TE},m}^c} \left(1 + \frac{\nu_{1\ell}^2}{2k^2 r_0^2} \right) \frac{r_0^2 J_1 \left(\frac{\nu_{1m}' a}{r_0} \right) J_1 \left(\frac{\nu_{1\ell} a}{r_0} \right)}{\nu_{1\ell} \nu_{1m}'} \quad (43)$$

Noticing that $A_0^- = 0$, since the incidence was purely TM in this case, we arrive at the total A_m^-

$$A_m^- = A_0^- + \tilde{A}_m^- = 0 + \tilde{A}_m^-$$

$$= - \frac{\pi B_\ell^{in} r_0^2 J_1 \left(\frac{\nu_{1m}' a}{r_0} \right) J_1 \left(\frac{\nu_{1\ell} a}{r_0} \right) \left(1 + \frac{\nu_{1\ell}^2}{2k^2 r_0^2} \right)}{2Z_0 \hat{P}_{\text{TE},m}^c \nu_{1\ell} \nu_{1m}'} \quad (44)$$

where

$$\hat{P}_{\text{TE},\ell}^c = \frac{1}{2} \iint^{r_0} r dr d\phi \hat{\mathbf{z}} \cdot (\hat{\mathbf{E}}_{\text{TE},\ell}^{+,c} \times \hat{\mathbf{H}}_{\text{TE},\ell}^{+,c}) \quad (45)$$

$$= \frac{\pi r_0^2}{4Z_0} \left(\frac{\nu_{1\ell}'^2}{2k^2 r_0^2} - 1 \right) \left(\frac{1}{\nu_{1\ell}'^2} - 1 \right) J_1^2(\nu_{1\ell}') \quad (46)$$

For *Scenario* (3), we find B_m^+ by utilizing \mathbf{E}_2 in (30) and calculating the LHS and RHS of (32), to yield

$$\oint_S (\mathbf{E}_2 \times \mathbf{H}_1 - \mathbf{E}_1 \times \mathbf{H}_2) \cdot d\mathbf{s} = 0 + 4B_m^+ \hat{P}_{\text{TM},m}^w = 4B_m^+ \hat{P}_{\text{TM},m}^w \quad (47)$$

$$\begin{aligned} & - \int_V dV \mathbf{E}_2 \cdot \mathbf{J}_1 = - \iiint^a r dr d\phi dz \left[\hat{\mathbf{E}}_{\text{TM},m}^{-,w} \cdot \left(2\hat{\mathbf{z}} \times \hat{\mathbf{H}}_{\text{TM},\ell}^{+,c} \right) B_\ell^{\text{in}} \delta(z) \right] \\ & = +2B_\ell^{\text{in}} \iiint^a r dr d\phi \left(\hat{E}_{r\text{TM},m}^{+,w} \hat{H}_{\phi\text{TM},\ell}^{+,c} - \hat{E}_{\phi\text{TM},m}^{+,w} \hat{H}_{r\text{TM},\ell}^{+,c} \right) \\ & = B_\ell^{\text{in}} \frac{2\pi}{Z_0} \left(1 + \frac{\nu_{1\ell}^2}{2k^2 r_0^2} \right) \int^a dr \left[r J_1' \left(\frac{\nu_{1m} r}{r_0} \right) J_1' \left(\frac{\nu_{1\ell} r}{r_0} \right) + \frac{a r_0}{\nu_{1\ell} r} J_1 \left(\frac{\nu_{1m} r}{r_0} \right) J_1 \left(\frac{\nu_{1\ell} r}{r_0} \right) \right] \\ & = B_\ell^{\text{in}} \frac{2\pi}{Z_0} \left(1 + \frac{\nu_{1\ell}^2}{2k^2 r_0^2} \right) \frac{a \nu_{1\ell} J_0(\nu_{1m}) J_1 \left(\frac{\nu_{1\ell} a}{r_0} \right)}{r_0 (\nu_{1\ell}^2 / r_0^2 - \nu_{1m}^2 / a^2)}, \end{aligned} \quad (48)$$

Upon equating (47) and (48), we obtain

$$B_m^+ = \frac{\pi B_\ell^{\text{in}} a \nu_{1\ell} J_0(\nu_{1m}) J_1 \left(\frac{\nu_{1\ell} a}{r_0} \right) \left(1 + \frac{\nu_{1\ell}^2}{2k^2 r_0^2} \right)}{2Z_0 \hat{P}_{\text{TM},m}^w r_0 (\nu_{1\ell}^2 / r_0^2 - \nu_{1m}^2 / a^2)} \quad (49)$$

Similarly, for *Scenario* (4), we find A_m^+ by utilizing \mathbf{E}_2 in (31) and calculating the LHS and RHS of (32), to yield

$$\begin{aligned} & \oint_S (\mathbf{E}_2 \times \mathbf{H}_1 - \mathbf{E}_1 \times \mathbf{H}_2) \cdot d\mathbf{s} = 0 + 4A_m^+ \hat{P}_{\text{TE},m}^w \quad (50) \\ & - \int_V dV \mathbf{E}_2 \cdot \mathbf{J}_1 \\ & = - \iiint^a r dr d\phi dz \left[\hat{\mathbf{E}}_{\text{TE},m}^{-,w} \cdot \left(2\hat{\mathbf{z}} \times \hat{\mathbf{H}}_{\text{TM},\ell}^{+,c} \right) B_\ell^{\text{in}} \delta(z) \right] \\ & = 2B_\ell^{\text{in}} \iiint^a r dr d\phi \left(\hat{E}_{r\text{TE},m}^{+,w} \hat{H}_{\phi\text{TM},\ell}^{+,c} - \hat{E}_{\phi\text{TE},m}^{+,w} \hat{H}_{r\text{TM},\ell}^{+,c} \right) \\ & = -B_\ell^{\text{in}} \frac{2\pi}{Z_0} \left(1 + \frac{\nu_{1\ell}^2}{2k^2 r_0^2} \right) \int^a dr \left[\frac{a}{\nu_{1m}'} J_1 \left(\frac{\nu_{1m}' r}{a} \right) \cdot \right. \\ & \quad \left. J_1' \left(\frac{\nu_{1\ell} r}{r_0} \right) + \frac{r_0}{\nu_{1\ell}} J_1' \left(\frac{\nu_{1m}' r}{a} \right) J_1 \left(\frac{\nu_{1\ell} r}{r_0} \right) \right] \\ & = -B_\ell^{\text{in}} \frac{2\pi}{Z_0} \left(1 + \frac{\nu_{1\ell}^2}{2k^2 r_0^2} \right) \frac{a r_0 J_0(\nu_{1m}') J_1 \left(\frac{\nu_{1\ell} a}{r_0} \right)}{\nu_{1\ell}} \end{aligned} \quad (51)$$

Upon equating (50) and (51), we obtain

$$A_m^+ = - \frac{\pi B_\ell^{\text{in}} a r_0 J_0(\nu_{1m}') J_1 \left(\frac{\nu_{1\ell} a}{r_0} \right) \left(1 + \frac{\nu_{1\ell}^2}{2k^2 r_0^2} \right)}{2Z_0 \hat{P}_{\text{TE},m}^w \nu_{1\ell}} \quad (52)$$

where

$$\hat{P}_{\text{TE},\ell}^w = \frac{1}{2} \iiint^a r dr d\phi \hat{\mathbf{z}} \cdot (\hat{\mathbf{E}}_{\text{TE},\ell}^{+,w} \times \hat{\mathbf{H}}_{\text{TE},\ell}^{+,w}) \quad (53)$$

$$= \frac{\pi a^2}{4Z_0} \left(\frac{\nu_{1\ell}^2}{2k^2 a^2} - 1 \right) \left(\frac{1}{\nu_{1\ell}^2} - 1 \right) J_1^2(\nu_{1\ell}') \quad (54)$$

To verify the correctness of the field expansions on both side of the discontinuity ($z = 0$), we use the coefficients derived in (40), (44), (49), and (52) in the transverse

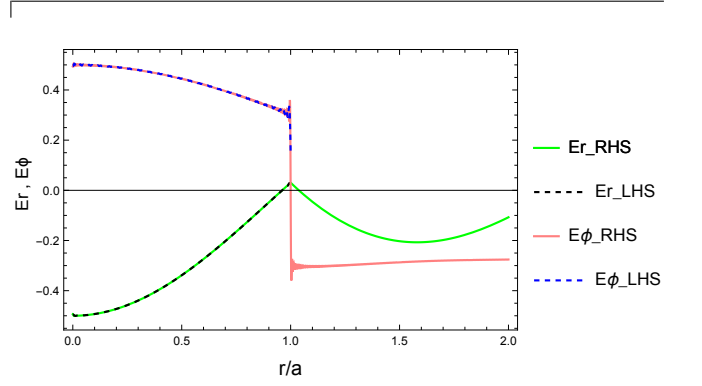


FIG. 5. Validating the match of each transverse field (E_r and E_ϕ) on the left-hand side and right-hand side of a step-in discontinuity, for TM incidence. The plot used the results in (40), (44), (49), and (52) for the field expansions, which were limited to 300 terms and plotted for an example structure that has $r_0/a = 2$.

fields E_r, E_ϕ , which should match at the $z = 0$ boundary. Figure 5 confirms the matching and the correctness of the results for a TM incidence on the step-in discontinuity.

C. Analysis of TM incidence on a step-out discontinuity

Following similar steps, one can show that, for a TM mode incident on a step-out discontinuity, the reflection coefficients are identically zero. The transmission coefficients for this case are therefore identical for the forward-scatter analysis reported in [15]. To formally prove this, we begin by writing the equivalent current source \mathbf{J}_1 for the incident more ($E_{\text{TM},\ell}^{\text{in},w}, H_{\text{TM},\ell}^{\text{in},w}$) and the reflected/transmitted ($\mathbf{E}_1, \mathbf{H}_1$) transverse field, to be used

in reciprocity theorem. Namely,

$$\mathbf{J}_1 = +\hat{n} \times \mathbf{H}_0 = \hat{n} \times 2\mathbf{H}_{\text{TM},\ell}^{in,w} = 2B_\ell^{in}\hat{n} \times \hat{\mathbf{H}}_{\text{TM},\ell}^{in,w} \quad (55)$$

$$\begin{aligned} \mathbf{E}_1^- &= \sum_n \mathbf{E}_{\text{TM},n}^{-,w} + \sum_n \mathbf{E}_{\text{TE},n}^{-,w} \\ &= \sum_n B_n^- \hat{\mathbf{E}}_{\text{TM},n}^{-,w} + \sum_n A_n^- \hat{\mathbf{E}}_{\text{TE},n}^{-,w} = \sum_n D_n^- \hat{\mathbf{E}}_n^{-,w} \end{aligned} \quad (56)$$

$$\begin{aligned} \mathbf{H}_1^- &= \sum_n \mathbf{H}_{\text{TM},n}^{-,w} + \sum_n \mathbf{H}_{\text{TE},n}^{-,w} \\ &= -\sum_n B_n^- \hat{\mathbf{H}}_{\text{TM},n}^{-,w} - \sum_n A_n^- \hat{\mathbf{H}}_{\text{TE},n}^{-,w} = -\sum_n D_n^- \hat{\mathbf{H}}_n^{-,w} \end{aligned} \quad (57)$$

$$\begin{aligned} \mathbf{E}_1^+ &= \sum_n \mathbf{E}_{\text{TM},n}^{+,c} + \sum_n \mathbf{E}_{\text{TE},n}^{+,c} \\ &= \sum_n B_n^+ \hat{\mathbf{E}}_{\text{TM},n}^{+,c} + \sum_n A_n^+ \hat{\mathbf{E}}_{\text{TE},n}^{+,c} = \sum_n D_n^+ \hat{\mathbf{E}}_n^{+,c} \end{aligned} \quad (58)$$

$$\begin{aligned} \mathbf{H}_1^+ &= \sum_n \mathbf{H}_{\text{TM},n}^{+,c} + \sum_n \mathbf{H}_{\text{TE},n}^{+,c} \\ &= -\sum_n B_n^+ \hat{\mathbf{H}}_{\text{TM},n}^{+,c} - \sum_n A_n^+ \hat{\mathbf{H}}_{\text{TE},n}^{+,c} = -\sum_n D_n^+ \hat{\mathbf{H}}_n^{+,c} \end{aligned} \quad (59)$$

For the normalized field \mathbf{E}_2 , we choose from the following four *scenarios*:

(1) to find B_m^- , take

$$\mathbf{E}_2 = \begin{cases} \hat{\mathbf{E}}_{\text{TM},m}^{+,w}, & z < 0 \\ \sum_p \alpha_{m,p}^+ \hat{\mathbf{E}}_p^{+,c}, & z > 0 \end{cases} \quad (60)$$

(2) To find A_m^- , take

$$\mathbf{E}_2 = \begin{cases} \hat{\mathbf{E}}_{\text{TE},m}^{+,w}, & z < 0 \\ \sum_p \beta_{m,p}^+ \hat{\mathbf{E}}_p^{+,c}, & z > 0 \end{cases} \quad (61)$$

(3) To find B_m^+ , take

$$\mathbf{E}_2 = \begin{cases} \sum_p \gamma_{m,p}^- \hat{\mathbf{E}}_p^{-,w}, & z < 0 \\ \hat{\mathbf{E}}_{\text{TM},m}^{-,c}, & z > 0 \end{cases} \quad (62)$$

(4) To find A_m^+ , take

$$\mathbf{E}_2 = \begin{cases} \sum_p \zeta_{m,p}^- \hat{\mathbf{E}}_p^{-,w}, & z < 0 \\ \hat{\mathbf{E}}_{\text{TE},m}^{-,c}, & z > 0 \end{cases} \quad (63)$$

Note that, in the above expressions, \mathbf{E}_p denotes both TE and TM modes, for brevity. The expansion coefficients (such as $\zeta_{m,p}^-$, for example) will thus include those for TE and TM modes. For example, one can write more explicitly $\sum_p \zeta_{m,p}^- \hat{\mathbf{E}}_p^{-,c}$ as $\sum_p B_{m,p}^- \hat{\mathbf{E}}_{\text{TM},p}^{-,c} + \sum_p A_{m,p}^- \hat{\mathbf{E}}_{\text{TE},p}^{-,c}$, and so forth.

For each of these scenarios, we can now use (55)–(59) in reciprocity theorem (32) to derive all the field coefficients analytically.

Consider *Scenario* (1) to find B_m^- by taking \mathbf{E}_2 from (60) in reciprocity theorem (32), and bearing in mind that $\oint_S \equiv \int_{S_1} + \int_{S_2}$. We find the LHS as

$$\begin{aligned} \int_{S_2} (\mathbf{E}_2 \times \mathbf{H}_1 - \mathbf{E}_1 \times \mathbf{H}_2) \cdot d\mathbf{s} &= - \iint^a r dr d\phi \hat{z} \cdot \left[\hat{\mathbf{E}}_{\text{TM},m}^{+,w} \times \sum_n D_n^- \hat{\mathbf{H}}_n^{-,w} - \sum_n D_n^- \hat{\mathbf{E}}_n^{-,w} \times \hat{\mathbf{H}}_{\text{TM},m}^{+,w} \right] \\ &= - \sum_n D_n^- \left[\iint^a r dr d\phi \hat{z} \cdot \left(\hat{\mathbf{E}}_{\text{TM},m}^{+,w} \times \hat{\mathbf{H}}_n^{-,w} \delta_{mn} - \hat{\mathbf{E}}_n^{-,w} \times \hat{\mathbf{H}}_{\text{TM},m}^{+,w} \delta_{mn} \right) \right] \\ &= -\tilde{B}_m^- \left[\iint^a r dr d\phi \hat{z} \cdot \left(-\hat{\mathbf{E}}_{\text{TM},m}^{+,w} \times \hat{\mathbf{H}}_{\text{TM},m}^{+,w} - \hat{\mathbf{E}}_{\text{TM},m}^{+,w} \times \hat{\mathbf{H}}_{\text{TM},m}^{+,w} \right) \right] \\ &= +2\tilde{B}_m^- \underbrace{\iint^a r dr d\phi \hat{z} \cdot (\hat{\mathbf{E}}_{\text{TM},m}^{+,w} \times \hat{\mathbf{H}}_{\text{TM},m}^{+,w})}_{=2\hat{P}_{\text{TM},m}^w} = +4\tilde{B}_m^- \hat{P}_{\text{TM},m}^w \end{aligned} \quad (64)$$

$$\begin{aligned} \int_{S_1} (\mathbf{E}_2 \times \mathbf{H}_1 - \mathbf{E}_1 \times \mathbf{H}_2) \cdot d\mathbf{s} &= + \iint^{r_0} r dr d\phi \hat{z} \cdot \left[\sum_p \alpha_{m,p}^+ \hat{\mathbf{E}}_p^{+,c} \times \sum_n D_n^+ \hat{\mathbf{H}}_n^{+,c} - \sum_n D_n^+ \hat{\mathbf{E}}_n^{+,c} \times \sum_p \alpha_{m,p}^+ \hat{\mathbf{H}}_p^{+,c} \right] \\ &= \sum_{n,p} \alpha_{m,p}^+ D_n^+ \iint^{r_0} r dr d\phi \hat{z} \cdot \left(\hat{\mathbf{E}}_p^{+,c} \times \hat{\mathbf{H}}_n^{+,c} - \hat{\mathbf{E}}_n^{+,c} \times \hat{\mathbf{H}}_p^{+,c} \right) = 0 \\ \Rightarrow \int_{S_1} + \int_{S_2} &\equiv \oint_S (\mathbf{E}_2 \times \mathbf{H}_1 - \mathbf{E}_1 \times \mathbf{H}_2) \cdot d\mathbf{s} = 0 + 4\tilde{B}_m^- \hat{P}_{\text{TM},m}^w = 4\tilde{B}_m^- \hat{P}_{\text{TM},m}^w \end{aligned} \quad (65)$$

On the other hand, the volume integral on the RHS of (32) gives

$$\begin{aligned}
-\int_V dV \mathbf{E}_2 \cdot \mathbf{J}_1 &= -\iiint^a r dr d\phi dz \left[\hat{\mathbf{E}}_{\text{TM},m}^{+,w} \cdot \left(2\hat{z} \times \hat{\mathbf{H}}_{\text{TM},\ell}^{+,w} \right) B_\ell^{in} \delta(z) \right] \\
&= +2B_\ell^{in} \iiint^a r dr d\phi \left(\hat{E}_{r\text{TM},m}^{+,w} \hat{H}_{\phi\text{TM},\ell}^{+,w} - \hat{E}_{\phi\text{TM},m}^{+,w} \hat{H}_{r\text{TM},\ell}^{+,w} \right) \\
&= +B_\ell^{in} \frac{2\pi}{Z_0} \left(1 + \frac{\nu_{1\ell}^2}{2k^2 a^2} \right) \int^a dr \left[r J_1' \left(\frac{\nu_{1m} r}{a} \right) J_1' \left(\frac{\nu_{1\ell} r}{a} \right) + \frac{a^2}{\nu_{1m} \nu_{1\ell} r} J_1 \left(\frac{\nu_{1m} r}{a} \right) J_1 \left(\frac{\nu_{1\ell} r}{a} \right) \right] \\
&= \frac{\pi B_\ell^{in}}{Z_0} \left(1 + \frac{\nu_{1\ell}^2}{2k^2 a^2} \right) \begin{cases} \frac{a^2}{2} [J_0^2(\nu_{1\ell}) + J_2^2(\nu_{1\ell})] = a^2 [J_0^2(\nu_{1\ell})], & m = \ell \\ 0, & m \neq \ell \end{cases} \quad (66)
\end{aligned}$$

where \tilde{B}_m^- denotes the coefficients of the TM mode scattered by the equivalent source \mathbf{J}_1 , and $\hat{P}_{\text{TM},m}^w$ denotes the complex power carried by the m th normalized TM mode from the waveguide section side.

Equating (66) and (65) now gives

$$\tilde{B}_m^- = \frac{\pi B_\ell^{in} \left(1 + \frac{\nu_{1\ell}^2}{2k^2 a^2} \right)}{4Z_0 \hat{P}_{\text{TM},m}^w} \begin{cases} a^2 J_0^2(\nu_{1\ell}), & m = \ell \\ 0, & m \neq \ell \end{cases} \quad (67)$$

Recall that this reflected field is only due to the equivalent source \mathbf{J}_1 . It needs to be added to the field due to the PEC filling, \mathbf{H}_0 , which has $B_0^- = B_\ell^{in} \delta_{m\ell}$, to give the total reflection. Thus, we arrive at the reflection coefficient

$$\begin{aligned}
B_m^- &= B_0^- + \tilde{B}_m^- = B_\ell^{in} \delta_{m\ell} + \tilde{B}_m^- \\
&= B_\ell^{in} \begin{cases} -1 + \frac{\pi a^2 J_0^2(\nu_{1\ell}) \left(1 + \frac{\nu_{1\ell}^2}{2k^2 a^2} \right)}{4Z_0 \hat{P}_{\text{TM},\ell}^w} = 0, & m = \ell \\ 0, & m \neq \ell \end{cases} \\
&= 0, \quad (68)
\end{aligned}$$

where we have used the fact that

$$\hat{P}_{\text{TM},\ell}^w = \frac{1}{2} \iiint^a r dr d\phi \hat{z} \cdot (\hat{\mathbf{E}}_{\text{TM},\ell}^{+,w} \times \hat{\mathbf{H}}_{\text{TM},\ell}^{+,w}) \quad (69)$$

$$= \frac{\pi a^2}{4Z_0} \left(1 + \frac{\nu_{1\ell}^2}{2k^2 a^2} \right) J_0^2(\nu_{1\ell}) \quad (70)$$

Applying *Scenario* (2) to find A_m^- , we use (61) in (32) to yield

$$\oint_S (\mathbf{E}_2 \times \mathbf{H}_1 - \mathbf{E}_1 \times \mathbf{H}_2) \cdot d\mathbf{s} = 0 + 4\tilde{A}_m^- P_{\text{TE},m}^w \quad (71)$$

$$\begin{aligned}
& - \int_V dV \mathbf{E}_2 \cdot \mathbf{J}_1 \\
&= -\iiint^a r dr d\phi dz \left[\hat{\mathbf{E}}_{\text{TE},m}^{+,w} \cdot \left(2\hat{z} \times \hat{\mathbf{H}}_{\text{TM},\ell}^{+,w} \right) B_\ell^{in} \delta(z) \right] \\
&= 2B_\ell^{in} \iiint^a r dr d\phi \left(\hat{E}_{r\text{TE},m}^{+,w} \hat{H}_{\phi\text{TM},\ell}^{+,w} - \hat{E}_{\phi\text{TE},m}^{+,w} \hat{H}_{r\text{TM},\ell}^{+,w} \right) \\
&= -B_\ell^{in} \frac{2\pi}{Z_0} \left(1 + \frac{\nu_{1\ell}^2}{2k^2 a^2} \right) \int^a dr \left[\frac{a}{\nu_{1m}} J_1 \left(\frac{\nu_{1m} r}{a} \right) \right. \\
&\quad \left. J_1' \left(\frac{\nu_{1\ell} r}{a} \right) + \frac{a}{\nu_{1\ell}} J_1' \left(\frac{\nu_{1m} r}{a} \right) J_1 \left(\frac{\nu_{1\ell} r}{a} \right) \right] = 0, \quad (72)
\end{aligned}$$

since the integral in (72) is a complete differential.

Upon equating (71) and (72), we obtain $\tilde{A}_m^- = 0$. Noticing that $A_0^- = 0$, since the incidence is purely TM in this case, we then arrive at

$$A_m^- = A_0^- + \tilde{A}_m^- = 0 + \tilde{A}_m^- = 0 \quad (73)$$

Applying *Scenario* (3) to find B_m^+ , we substitute from (62) into reciprocity theorem (32) to yield

$$\oint_S (\mathbf{E}_2 \times \mathbf{H}_1 - \mathbf{E}_1 \times \mathbf{H}_2) \cdot d\mathbf{s} = 0 + 4B_m^+ \hat{P}_{\text{TM},m}^c \quad (74)$$

$$\begin{aligned}
& - \int_V dV \mathbf{E}_2 \cdot \mathbf{J}_1 \\
&= -\iiint^a r dr d\phi dz \left[\hat{\mathbf{E}}_{\text{TM},m}^{-,c} \cdot \left(2\hat{z} \times \hat{\mathbf{H}}_{\text{TM},\ell}^{+,w} \right) B_\ell^{in} \delta(z) \right] \\
&= 2B_\ell^{in} \iiint^a r dr d\phi \left(\hat{E}_{r\text{TM},m}^{-,c} \hat{H}_{\phi\text{TM},\ell}^{+,w} - \hat{E}_{\phi\text{TM},m}^{-,c} \hat{H}_{r\text{TM},\ell}^{+,w} \right) \\
&= B_\ell^{in} \frac{2\pi}{Z_0} \left(1 + \frac{\nu_{1\ell}^2}{2k^2 a^2} \right) \int^a dr \left[r J_1' \left(\frac{\nu_{1m} r}{r_0} \right) \right. \\
&\quad \left. J_1' \left(\frac{\nu_{1\ell} r}{r_0} \right) + \frac{a r_0}{\nu_{1\ell} \nu_{1m} r} J_1 \left(\frac{\nu_{1m} r}{r_0} \right) J_1 \left(\frac{\nu_{1\ell} r}{r_0} \right) \right] \quad (75)
\end{aligned}$$

$$= B_\ell^{in} \left(1 + \frac{\nu_{1\ell}^2}{2k^2 a^2} \right) \frac{2\pi a \nu_{1m} J_0(\nu_{1\ell}) J_1 \left(\nu_{1m} \frac{a}{r_0} \right)}{Z_0 r_0 (\nu_{1m}^2 / r_0^2 - \nu_{1\ell}^2 / a^2)} \quad (76)$$

Upon equating (74) and (76), we obtain

$$B_m^+ = \frac{\pi B_\ell^{in}}{2Z_0 \hat{P}_{\text{TM},m}^c} \left(1 + \frac{\nu_{1\ell}^2}{2k^2 a^2} \right) \frac{a \nu_{1m} J_0(\nu_{1\ell}) J_1 \left(\nu_{1m} \frac{a}{r_0} \right)}{r_0 (\nu_{1m}^2 / r_0^2 - \nu_{1\ell}^2 / a^2)}. \quad (77)$$

where

$$\hat{P}_{\text{TM},\ell}^c = \pi r_0^2 \left(1 + \frac{\nu_{1\ell}^2}{2k^2 r_0^2} \right) J_0^2(\nu_{1\ell}) / (4Z_0) \quad (78)$$

We use *Scenario* (4) to find A_m^+ , by using (63) in (32)

and following the same steps. We find

$$\begin{aligned}
\oint_S (\mathbf{E}_2 \times \mathbf{H}_1 - \mathbf{E}_1 \times \mathbf{H}_2) \cdot d\mathbf{s} &= 0 + 4A_m^+ P_{\text{TE},m}^c \quad (79) \\
- \int_V dV \mathbf{E}_2 \cdot \mathbf{J}_1 \\
&= - \iiint^a r dr d\phi dz \left[\hat{\mathbf{E}}_{\text{TE},m}^{-,c} \cdot \left(2\hat{z} \times \hat{\mathbf{H}}_{\text{TM},\ell}^{+,w} \right) B_\ell^{in} \delta(z) \right] \\
&= 2B_\ell^{in} \iiint^a r dr d\phi \left(\hat{E}_{r\text{TE},m}^{+,c} \hat{H}_{\phi\text{TM},\ell}^{+,w} - \hat{E}_{\phi\text{TE},m}^{+,c} \hat{H}_{r\text{TM},\ell}^{+,w} \right) \\
&= -B_\ell^{in} \frac{2\pi}{Z_0} \left(1 + \frac{\nu_{1\ell}^2}{2k^2 a^2} \right) \int^a dr \left[\frac{r_0}{\nu_{1m}'} J_1 \left(\frac{\nu_{1m}' r}{r_0} \right) \right. \\
&\quad \left. J_1' \left(\frac{\nu_{1\ell} r}{a} \right) + \frac{a}{\nu_{1\ell}} J_1' \left(\frac{\nu_{1m}' r}{r_0} \right) J_1 \left(\frac{\nu_{1\ell} r}{a} \right) \right] = 0, \quad (80)
\end{aligned}$$

since the integral in (80) is a complete differential.

Upon equating (79) and (80), we obtain

$$A_m^+ = 0. \quad (81)$$

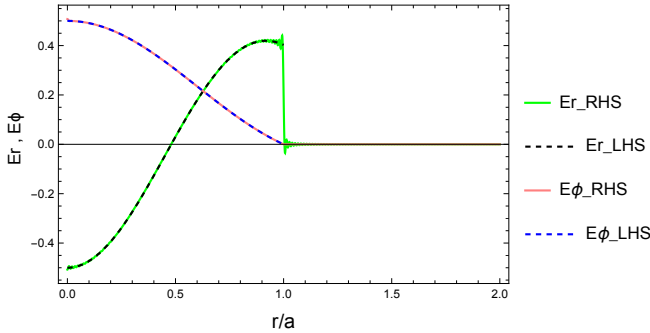


FIG. 6. Validating the match of each transverse field (E_r and E_ϕ) on the left-hand side and right-hand side of a step-out discontinuity, for TM incidence. The plot used the results in (68), (73), (77), and (81) for the field expansions, which were limited to 300 terms and plotted for an example structure that has $r_0/a = 2$.

To verify the correctness of the field expansions on both side of the discontinuity ($z = 0$), we use the coefficients derived in (68), (73), (77), and (81) in the transverse fields E_r, E_ϕ , which should match at the $z = 0$ boundary. Figure 6 confirms the matching and the correctness of the results for a TM incidence on the step-in discontinuity.

For brevity, and since the same approach is reused to find the analysis for the TE incidence on step-in and step-out discontinuity, Subsections IID and IIE will mainly summarize the key field equations and the resulting coefficients.

D. Analysis of TE incidence on a step-in discontinuity

Following similar steps for the case with TE incidence, ($E_{\text{TE},\ell}^{in,c}, H_{\text{TE},\ell}^{in,c}$), on a step-in discontinuity, we can write the equivalent current source \mathbf{J}_1 and $(\mathbf{E}_1, \mathbf{H}_1)$ fields as

$$\begin{aligned}
\mathbf{J}_1 &= +\hat{n} \times \mathbf{H}_0 = +\hat{n} \times 2\mathbf{H}_{\text{TE},\ell}^{in,c} = 2A_\ell^{in} \hat{n} \times \hat{\mathbf{H}}_{\text{TE},\ell}^{in,c} \quad (82) \\
\mathbf{E}_1^- &= \sum_n \mathbf{E}_{\text{TM},n}^{-,c} + \sum_n \mathbf{E}_{\text{TE},n}^{-,c} \\
&= \sum_n B_n^- \hat{\mathbf{E}}_{\text{TM},n}^{+,c} + \sum_n A_n^- \hat{\mathbf{E}}_{\text{TE},n}^{+,c} = \sum_n D_n^- \hat{\mathbf{E}}_n^{+,c} \\
\mathbf{H}_1^- &= \sum_n \mathbf{H}_{\text{TM},n}^{-,c} + \sum_n \mathbf{H}_{\text{TE},n}^{-,c} \\
&= -\sum_n B_n^- \hat{\mathbf{H}}_{\text{TM},n}^{+,c} - \sum_n A_n^- \hat{\mathbf{H}}_{\text{TE},n}^{+,c} = -\sum_n D_n^- \hat{\mathbf{H}}_n^{+,c} \quad (83)
\end{aligned}$$

$$\begin{aligned}
\mathbf{E}_1^+ &= \sum_n \mathbf{E}_{\text{TM},n}^{+,w} + \sum_n \mathbf{E}_{\text{TE},n}^{+,w} \\
&= \sum_n B_n^+ \hat{\mathbf{E}}_{\text{TM},n}^{+,w} + \sum_n A_n^+ \hat{\mathbf{E}}_{\text{TE},n}^{+,w} = \sum_n D_n^+ \hat{\mathbf{E}}_n^{+,w} \\
\mathbf{H}_1^+ &= \sum_n \mathbf{H}_{\text{TM},n}^{+,w} + \sum_n \mathbf{H}_{\text{TE},n}^{+,w} \\
&= -\sum_n B_n^+ \hat{\mathbf{H}}_{\text{TM},n}^{+,w} - \sum_n A_n^+ \hat{\mathbf{H}}_{\text{TE},n}^{+,w} = -\sum_n D_n^+ \hat{\mathbf{H}}_n^{+,w} \quad (84)
\end{aligned}$$

The normalized field \mathbf{E}_2 is chosen out of the following four scenarios, to find the four coefficient sets:

(1) To find B_m^- , take

$$\mathbf{E}_2 = \begin{cases} \hat{\mathbf{E}}_{\text{TM},m}^{+,c}, & z < 0 \\ \sum_p \alpha_{m,p}^+ \hat{\mathbf{E}}_p^{+,w}, & z > 0 \end{cases} \quad (85)$$

(2) To find A_m^- , take

$$\mathbf{E}_2 = \begin{cases} \hat{\mathbf{E}}_{\text{TE},m}^{+,c}, & z < 0 \\ \sum_p \beta_{m,p}^+ \hat{\mathbf{E}}_p^{+,w}, & z > 0 \end{cases} \quad (86)$$

(3) To find B_m^+ , take

$$\mathbf{E}_2 = \begin{cases} \sum_p \gamma_{m,p}^- \hat{\mathbf{E}}_p^{-,c}, & z < 0 \\ \hat{\mathbf{E}}_{\text{TM},m}^{-,w}, & z > 0 \end{cases} \quad (87)$$

(4) To find A_m^+ , take

$$\mathbf{E}_2 = \begin{cases} \sum_p \zeta_{m,p}^- \hat{\mathbf{E}}_p^{-,c}, & z < 0 \\ \hat{\mathbf{E}}_{\text{TE},m}^{-,w}, & z > 0 \end{cases} \quad (88)$$

Using (82)–(84) and scenarios (85)–(88) in reciprocity theorem (32), we arrive, after mathematical reduction, at the following coefficients

$$B_m^- = \frac{\pi A_\ell^{in} r_0^2 J_1(\nu_{1m} \frac{a}{r_0}) J_1 \left(\nu_{1\ell}' \frac{a}{r_0} \right) \left(\frac{\nu_{1\ell}'^2}{2k^2 r_0^2} - 1 \right)}{2Z_0 \hat{P}_{\text{TM},m}^c \nu_{1\ell}' \nu_{1m}} \quad (89)$$

$$A_m^- = A_0^- + \tilde{A}_m^- = A_\ell^{in} \delta_{m\ell} + \tilde{A}_m^- = A_\ell^{in} \begin{cases} -1 + \frac{-\pi}{4Z_0 \tilde{P}_{TE,m}^c} \left(\frac{\nu_{1\ell}^{\prime 2}}{2k^2 r_0^2} - 1 \right) \hat{\Psi}_1, & m = \ell \\ \frac{-\pi}{4Z_0 \tilde{P}_{TE,m}^c} \left(\frac{\nu_{1\ell}^{\prime 2}}{2k^2 r_0^2} - 1 \right) \hat{\Psi}_2, & m \neq \ell \end{cases}, \text{ where} \quad (90)$$

$$\hat{\Psi}_1 = \frac{a^2}{2} \left[J_0^2 \left(\frac{\nu_{1\ell}' a}{r_0} \right) + J_1^2 \left(\frac{\nu_{1\ell}' a}{r_0} \right) + J_2^2 \left(\frac{\nu_{1\ell}' a}{r_0} \right) - J_1 \left(\frac{\nu_{1\ell}' a}{r_0} \right) J_3 \left(\frac{\nu_{1\ell}' a}{r_0} \right) \right] \quad (91)$$

$$\hat{\Psi}_2 = \frac{ar_0}{\nu_{1\ell}^{\prime 2} - \nu_{1m}^{\prime 2}} \left\{ \nu_{1\ell}' J_1 \left(\frac{\nu_{1\ell}' a}{r_0} \right) \left[J_0 \left(\frac{\nu_{1m}' a}{r_0} \right) - J_2 \left(\frac{\nu_{1m}' a}{r_0} \right) \right] + \nu_{1m}' J_1 \left(\frac{\nu_{1m}' a}{r_0} \right) \left[J_2 \left(\frac{\nu_{1\ell}' a}{r_0} \right) - J_0 \left(\frac{\nu_{1\ell}' a}{r_0} \right) \right] \right\} \quad (92)$$

$$B_m^+ = 0 \quad (93)$$

$$A_m^+ = \frac{-\pi A_\ell^{in} r_0^2 \nu_{1m}' J_1(\nu_{1m}') J_1' \left(\nu_{1\ell}' \frac{a}{r_0} \right) \left(\frac{\nu_{1\ell}^{\prime 2}}{2k^2 r_0^2} - 1 \right)}{2Z_0 P_{TE,m}^w (\nu_{1m}'^2 r_0^2 / a^2 - \nu_{1\ell}'^2)} \quad (94)$$

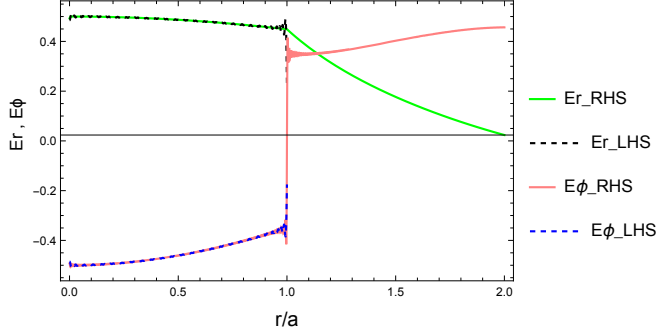


FIG. 7. Validating the match of each transverse field (E_r and E_ϕ) on the left-hand side and right-hand side of a step-in discontinuity, for TE incidence. The plot used the results in (89), (90), (93), and (94) for the field expansions, which were limited to 300 terms and plotted for an example structure that has $r_0/a = 2$.

To verify the correctness of the field expansions on both side of the discontinuity ($z = 0$), we use the coefficients derived in (89), (90), (93), and (94) in the transverse fields E_r , E_ϕ , which should match at the $z = 0$ boundary. Figure 7 confirms the matching and the correctness of the results for a TE incidence on the step-in discontinuity.

E. Analysis of TE incidence on a step-out discontinuity

Conducting the same analysis steps for a TE incidence, ($E_{TE,\ell}^{in,c}$, on a step-out will lead to reflection coefficients are identically zero. The transmission coefficients for this case are therefore identical for the forward-scatter analysis reported in [15]. We can write the equivalent current

source \mathbf{J}_1 and $(\mathbf{E}_1, \mathbf{H}_1)$ fields as

$$\mathbf{J}_1 = +\hat{n} \times \mathbf{H}_0 = \hat{n} \times 2\mathbf{H}_{TE,\ell}^{in,w} = 2A_\ell^{in} \hat{n} \times \hat{\mathbf{H}}_{TE,\ell}^{in,w} \quad (95)$$

$$\begin{aligned} \mathbf{E}_1^- &= \sum_n \mathbf{E}_{TM,n}^{-,w} + \sum_n \mathbf{E}_{TE,n}^{-,w} \\ &= \sum_n B_n^- \hat{\mathbf{E}}_{TM,n}^{+,w} + \sum_n A_n^- \hat{\mathbf{E}}_{TE,n}^{+,w} = \sum_n D_n^- \hat{\mathbf{E}}_n^{+,w} \\ \mathbf{H}_1^- &= \sum_n \mathbf{H}_{TM,n}^{-,w} + \sum_n \mathbf{H}_{TE,n}^{-,w} \\ &= -\sum_n B_n^- \hat{\mathbf{H}}_{TM,n}^{+,w} - \sum_n A_n^- \hat{\mathbf{H}}_{TE,n}^{+,w} = -\sum_n D_n^- \hat{\mathbf{H}}_n^{+,w} \end{aligned} \quad (96)$$

$$\begin{aligned} \mathbf{E}_1^+ &= \sum_n \mathbf{E}_{TM,n}^{+,c} + \sum_n \mathbf{E}_{TE,n}^{+,c} \\ &= \sum_n B_n^+ \hat{\mathbf{E}}_{TM,n}^{+,c} + \sum_n A_n^+ \hat{\mathbf{E}}_{TE,n}^{+,c} = \sum_n D_n^+ \hat{\mathbf{E}}_n^{+,c} \\ \mathbf{H}_1^+ &= \sum_n \mathbf{H}_{TM,n}^{+,c} + \sum_n \mathbf{H}_{TE,n}^{+,c} \\ &= -\sum_n B_n^+ \hat{\mathbf{H}}_{TM,n}^{+,c} - \sum_n A_n^+ \hat{\mathbf{H}}_{TE,n}^{+,c} = -\sum_n D_n^+ \hat{\mathbf{H}}_n^{+,c} \end{aligned} \quad (97)$$

The normalized field \mathbf{E}_2 is chosen out of the following four scenarios, to find the four coefficient sets:

(1) To find B_m^- , take

$$\mathbf{E}_2 = \begin{cases} \hat{\mathbf{E}}_{TM,m}^{+,w}, & z < 0 \\ \sum_p \alpha_{m,p}^+ \hat{\mathbf{E}}_p^{+,c}, & z > 0 \end{cases} \quad (98)$$

(2) To find A_m^- , take

$$\mathbf{E}_2 = \begin{cases} \hat{\mathbf{E}}_{TE,m}^{+,w}, & z < 0 \\ \sum_p \beta_{m,p}^+ \hat{\mathbf{E}}_p^{+,c}, & z > 0 \end{cases} \quad (99)$$

(3) To find B_m^+ , take

$$\mathbf{E}_2 = \begin{cases} \sum_p \gamma_{m,p}^- \hat{\mathbf{E}}_p^{-,w}, & z < 0 \\ \hat{\mathbf{E}}_{TM,m}^{-,c}, & z > 0 \end{cases} \quad (100)$$

(4) To find A_m^+ , take

$$\mathbf{E}_2 = \begin{cases} \sum_p \zeta_{m,p}^- \hat{\mathbf{E}}_p^{-,w}, & z < 0 \\ \hat{\mathbf{E}}_{TE,m}^{-,c}, & z > 0 \end{cases} \quad (101)$$

Using (95)–(97) and scenarios (II E)–(101) in reciprocity theorem (32), we arrive, after mathematical reduction, at the following coefficients

$$B_m^- = 0 \quad (102)$$

$$A_m^- = 0 \quad (103)$$

$$B_m^+ = \frac{\pi A_\ell^{in} a r_0 J_1\left(\frac{\nu_{1m} a}{r_0}\right) J_1(\nu_{1\ell}') \left(\frac{\nu_{1\ell}'^2}{2k^2 a^2} - 1\right)}{2Z_0 \hat{P}_{\text{TM},m}^c \nu_{1\ell}' \nu_{1m}} \quad (104)$$

$$A_m^+ = \frac{\pi A_\ell^{in} r_0^2 \nu_{1\ell}' J_1(\nu_{1\ell}') J_1'\left(\nu_{1m}' \frac{a}{r_0}\right) \left(1 - \frac{\nu_{1\ell}'^2}{2k^2 a^2}\right)}{2Z_0 \hat{P}_{\text{TE},m}^c (\nu_{1\ell}'^2 r_0^2 / a^2 - \nu_{1m}'^2)} \quad (105)$$

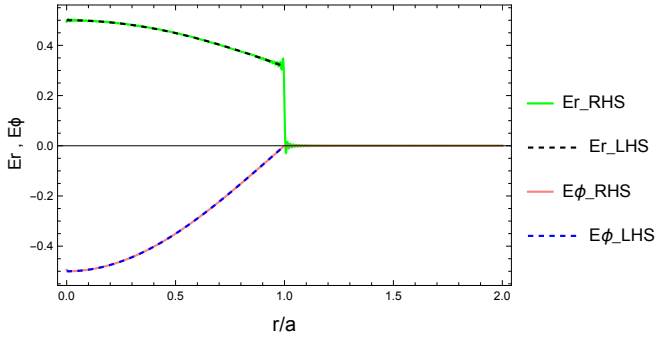


FIG. 8. Validating the match of each transverse field (E_r and E_ϕ) on the left-hand side and right-hand side of a step-out discontinuity, for TE incidence. The plot used the results in (102), (103), (104), and (105) for the field expansions, which were limited to 300 terms and plotted for an example structure that has $r_0/a = 2$.

To verify the correctness of the field expansions on both side of the discontinuity ($z = 0$), we use the coefficients derived in (102), (103), (104), and (105) in the transverse fields E_r , E_ϕ , which should match at the $z = 0$ boundary. Figure 8 confirms the matching and the correctness of the results for a TE incidence on the step-out discontinuity.

F. Summary of full-scatter coefficients

The results obtained in Subsections II B–II E can now be summarized as follows, where the acronyms “SI” and “SO” stand for step-in and step-out, respectively.

$$B_m^- = \begin{cases} \frac{\pi B_\ell^{in} \left(1 + \frac{\nu_{1\ell}'^2}{2k^2 r_0^2}\right)}{4Z_0 \hat{P}_{\text{TM},m}^c} \begin{cases} \Psi_1, & m = \ell \\ \Psi_2, & m \neq \ell \end{cases}, & \text{TM}_\ell^{\text{SI}} \\ 0, & \text{TM}_\ell^{\text{SO}} \\ \frac{\pi A_\ell^{in} r_0^2 J_1(\nu_{1m}' \frac{a}{r_0}) J_1(\nu_{1\ell}' \frac{a}{r_0}) \left(\frac{\nu_{1\ell}'^2}{2k^2 r_0^2} - 1\right)}{2Z_0 \hat{P}_{\text{TM},m}^c \nu_{1\ell}' \nu_{1m}}, & \text{TE}_\ell^{\text{SI}} \\ 0, & \text{TE}_\ell^{\text{SO}} \end{cases} \quad (106)$$

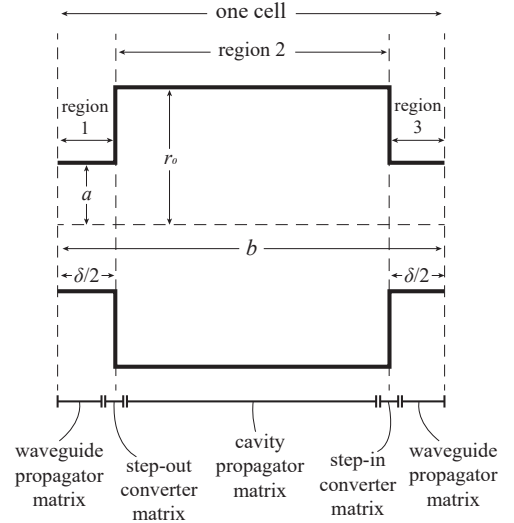


FIG. 9. A sketch illustrating a cell in the iris line, and how the different sections of the cell are modelled using different transmission matrices in the numerical analysis.

$$A_m^- = \begin{cases} -\frac{\pi B_\ell^{in} r_0^2 J_1\left(\frac{\nu_{1m}'}{r_0}\right) J_1\left(\frac{\nu_{1\ell}'}{r_0}\right) \left(1 + \frac{\nu_{1\ell}'^2}{2k^2 r_0^2}\right)}{2Z_0 \hat{P}_{\text{TE},m}^c \nu_{1\ell}' \nu_{1m}}, & \text{TM}_\ell^{\text{SI}} \\ 0, & \text{TM}_\ell^{\text{SO}} \\ -A_\ell^{in} + \frac{-\pi A_\ell^{in} \left(\frac{\nu_{1\ell}'^2}{2k^2 r_0^2} - 1\right)}{4Z_0 \hat{P}_{\text{TE},m}^c} \hat{\Psi}_1, & m = \ell \\ \frac{-\pi A_\ell^{in} \left(\frac{\nu_{1\ell}'^2}{2k^2 r_0^2} - 1\right)}{4Z_0 \hat{P}_{\text{TE},m}^c} \hat{\Psi}_2, & m \neq \ell \\ 0, & \text{TE}_\ell^{\text{SI}} \\ 0, & \text{TE}_\ell^{\text{SO}} \end{cases} \quad (107)$$

$$B_m^+ = \begin{cases} \frac{\pi B_\ell^{in} a \nu_{1\ell}' J_0(\nu_{1m}) J_1\left(\frac{\nu_{1\ell}'}{r_0}\right) \left(1 + \frac{\nu_{1\ell}'^2}{2k^2 r_0^2}\right)}{2Z_0 \hat{P}_{\text{TM},m}^w r_0 (\nu_{1\ell}'^2 / r_0^2 - \nu_{1m}'^2 / a^2)}, & \text{TM}_\ell^{\text{SI}} \\ \frac{\pi B_\ell^{in} a \nu_{1m}' J_0(\nu_{1\ell}') J_1\left(\nu_{1m}' \frac{a}{r_0}\right) \left(1 + \frac{\nu_{1\ell}'^2}{2k^2 a^2}\right)}{2Z_0 \hat{P}_{\text{TM},m}^c r_0 (\nu_{1m}'^2 / r_0^2 - \nu_{1\ell}'^2 / a^2)}, & \text{TM}_\ell^{\text{SO}} \\ 0, & \text{TE}_\ell^{\text{SI}} \\ \frac{\pi A_\ell^{in} a r_0 J_1\left(\frac{\nu_{1m}'}{r_0}\right) J_1(\nu_{1\ell}') \left(\frac{\nu_{1\ell}'^2}{2k^2 a^2} - 1\right)}{2Z_0 \hat{P}_{\text{TM},m}^c \nu_{1\ell}' \nu_{1m}}, & \text{TE}_\ell^{\text{SO}} \end{cases} \quad (108)$$

$$A_m^+ = \begin{cases} -\frac{\pi B_\ell^{in} a r_0 J_0(\nu_{1m}') J_1\left(\frac{\nu_{1\ell}'}{r_0}\right) \left(1 + \frac{\nu_{1\ell}'^2}{2k^2 r_0^2}\right)}{2Z_0 \hat{P}_{\text{TE},m}^w \nu_{1\ell}'}, & \text{TM}_\ell^{\text{SI}} \\ 0, & \text{TM}_\ell^{\text{SO}} \\ -\pi A_\ell^{in} r_0^2 \nu_{1m}' J_1(\nu_{1m}') J_1'\left(\nu_{1\ell}' \frac{a}{r_0}\right) \left(\frac{\nu_{1\ell}'^2}{2k^2 r_0^2} - 1\right), & \text{TE}_\ell^{\text{SI}} \\ \frac{\pi A_\ell^{in} r_0^2 \nu_{1\ell}' J_1(\nu_{1\ell}') J_1'\left(\nu_{1m}' \frac{a}{r_0}\right) \left(1 - \frac{\nu_{1\ell}'^2}{2k^2 a^2}\right)}{2Z_0 \hat{P}_{\text{TE},m}^c (\nu_{1\ell}'^2 r_0^2 / a^2 - \nu_{1m}'^2)}, & \text{TE}_\ell^{\text{SO}} \end{cases} \quad (109)$$

where $\Psi_{1,2}$ are given in given by (36) and (37), $\hat{\Psi}_{1,2}$ are given in given by (91) and (92), and $\hat{P}_{\text{TM},m}^c$, $\hat{P}_{\text{TE},m}^c$, $\hat{P}_{\text{TM},m}^w$, $\hat{P}_{\text{TE},m}^w$ are given, respectively, by (78), (45), (69) and (53)

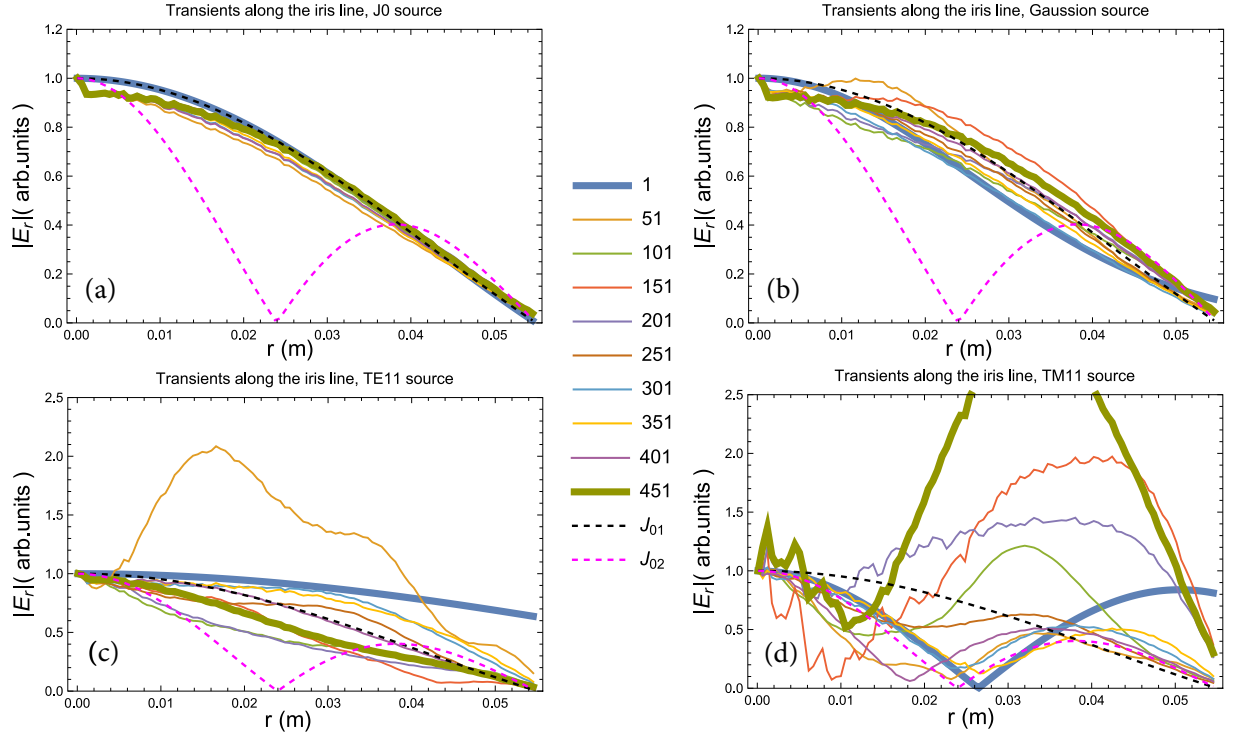


FIG. 10. Normalized E_r field transients evolving along the iris line toward steady state. For clarity, the fields are samples every 50 irises, on the iris numbers shown in the middle of the figure (the heavy blue trace indicates the first iris, and the heavy green trace represents that last iris). Also shows are the ideal (reference) curves of the first two J_0 modes, at the first and second zeros of J_0 . Different excitation scenarios are shown: (a) the backed-off Gaussian source, (b) a well-matched $J_0(2.4r/a)$ source, (c) a TE_{11} source, and (d) a TM_{11} source. See further discussion in the text.

III. IMPLEMENTATION AND NUMERICAL EXAMPLES

The theoretical findings for the full-scatter analysis developed in Section II are now implemented on a computer, to solve for numerical examples and to benchmark the results against other known models. The iris line is divided into cells, as shown in Figure 9, where each cell is represented by a cell transmission matrix C and the entire line is made up by cascading a number of such cells [15]. The total scattering matrix of the line is therefore the multiplication of multiple cell matrices, in their order of occurrence. As described in [15], each cell matrix is found by modeling the cell by 5 submatrices, representing a propagator matrix (P_1) for waveguide region 1, followed by a step-out scattering matrix ($S_{\text{step-out}}$), a propagator matrix (P_2) in cavity region 2, a step-in scattering matrix ($S_{\text{step-in}}$), and finally a propagator matrix (P_3) in waveguide region 3; see Figure 9. As an example, the output vector matrix $E_{r,\text{out}}^T$, representing the E_r field TE and TM modes scattered by a cell, for a given input vector $E_{r,\text{in}}^T$, is given by

$$E_{r,\text{out}}^T = E_{r,\text{in}}^T \cdot \underbrace{P_1 \cdot S_{\text{step-out}} \cdot P_2 \cdot S_{\text{step-in}} \cdot P_3}_{\equiv C}, \quad (110)$$

where the superscript T denoted the matrix transpose. The scattering (or “converter”) matrices are populated with the coefficients we derived in Section II and summarized in (106)–(109). For full details on the construction of these matrices, the reader is referred to reference [15].

This scattering formulation has a higher computational efficiency compared to standard finite-elements methods (FEM) or the eigensolution method developed in [14], for the overmoded structures under considerations. In addition to lending itself to structures that are not fully periodic (e.g. mechanical defects represent slightly different matrices), this method allows us to observe the extent of the transient regime that happens at the entrance of the iris line, as we excite the structure by a given source. We will also benchmark the results of this full-scatter analysis against the Vainstein limit for thin screens ($\delta \rightarrow 0$) [9, 11, 13, 22], the eigensolution method [14], and the high-frequency forward-scattering theory [15], demonstrating good agreement. In addition to representing an extension of the forward-scatter theory by including the reflected waves, this theory helps to confirm the validity of the forward-scatter approximation [15] for the analysis of overmoded structures.

Given the diffractive nature of the iris line and the shortness of a single-pass THz pulse (ignoring any secondary echoes), the diffraction loss is estimated by finding the ratio of the power scattered forward (down the

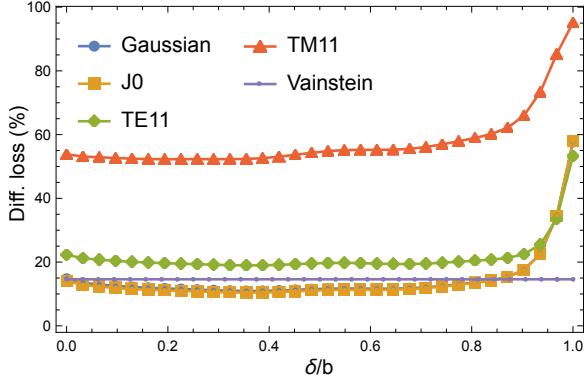


FIG. 11. Behavior of diffraction loss as a function of screen thickness δ , for four types of excitations: $J_0(2.4r/a)$, backed-off Gaussian, TE₁₁, and TM₁₁.

line) to the power incident from the source [15]. The part of the signal power that is scattered into the shadow regions between the screens is thus equivalent to what is “lost” to diffraction. The need to include practical screen thicknesses with conductive walls and chambers necessitate incorporating the effects of ohmic loss in the signal’s path, which tends to increase with increasing screen thickness δ , due to the presence of azimuthal and longitudinal surfaces currents on the iris rims. By using vector fields, the theory developed in Section II allows us to include the effects of diffractive and ohmic losses.

Given the thin skin layer for good conductors at THz frequencies, the ohmic loss is found on each screen rim (of width δ) using the traditional perturbation technique, which uses the tangential magnetic field when the surface is assumed to be a perfect conductor [1, 4, 5, 7, 23]. Namely, the power loss per unit length along the axial direction is given by

$$p' = \frac{R_s}{2} \int_0^{2\pi} [|H_\phi(a, \phi, z)|^2 + |H_z(a, \phi, z)|^2] a d\phi, \quad (111)$$

where $R_s = \sqrt{kZ_0/2\sigma}$ is the skin depth and σ is the conductivity of the screen edge. It is important to know that the total magnetic fields, H_ϕ and H_z in (111), are the sums that include all the modal terms of each field, $\sum_n H_{n\phi}^\pm$ and $\sum_n H_{nz}^\pm$. Finding their square magnitude will therefore include cross-terms among all modes, which will allow the difference TE/TM modes to interfere together, adding to or canceling each others’ surface current contributions. Note that equations (107)–(110) in reference [15] have an error, as the individual mode TE and TM mode contributions are not isolated in this overmoded structure. This can be simply corrected by accounting for the sum of terms before taking the square magnitudes; i.e., $|\sum_n H_{n\phi}^\pm|^2$ and $|\sum_n H_{nz}^\pm|^2$.

In the following numerical examples, we will take the example of a canonical structure with dimensions $a = 55$ cm, $b = 33.3$ cm, $r_0 = 2a$, and a total line length of 150 m (equivalent to approximately 451 irises), which is a candidate iris-line structure for THz radiation transport

at the SLAC National Accelerator Laboratory, Stanford University [13–16]. Since the diffraction loss is most severe at the lower frequency end of the operating range (3–15 THz), we study the 3 THz frequency ($\lambda = 0.1$ mm) and we limit all our modal sums to 500 terms. We will also observe the field output at consecutive cells in order to examine the effect of mode-launching purity for different sources and how the the excited fields gradually settle down toward the steady state of the structure. When the excitation is well matched to the structure’s dominant eigenmode, mode purity is high and we observe the field settling to the steady state over a relatively short distance, with a desirable profile similar to the $J_0(2.4r/a)$ form and a uniformly linear polarization across the iris [14, 15]. If the source is mismatched, however, the signal, which is represented as a linear superposition of eigenmodes, will encourage mode competition within the structure, which will take longer to settle down to the desired mode at the output of the iris line. This is demonstrated by four excitation scenarios.

A. Well-matched J_0 source

Exciting the first iris of the line by Bessel source with a dipolar transverse E field profile of the form $J_0(2.4r/a)$ represents an excitation that is well-matched to the ideal eigenmode (steady state) of the structure in the Vainstein limit. The latter limit occurs when the structure is oversized (overmoded) with a large Fresnel number, $N_f = a^2/(\lambda b) \gg 1$, and very thin screens, $\delta \rightarrow 0$, which leads to a transverse E field [9, 13] of the desirable form

$$J_0 \left[(1 - \varepsilon - i\varepsilon) \frac{2.4r}{a} \right], \quad (112)$$

where $\varepsilon \approx 0.164\sqrt{\lambda b}/a$ and is assumed small ($\varepsilon \ll 1$) in Vainstein’s limit. This profile is akin to the $J_0(2.4r/a)$ profile, but with a small perturbation ε that enters through its complex argument. The latter is a key feature of this geometry and represents the complex-impedance boundary condition (also named Vainstein’s impedance condition [13–15]) that is equivalent to the structure’s periodic nature, which enables the modes to mix and become hybrid in the axial region $r \leq a$. Therefore, this excitation is expected to have the shortest transient regime, with the mode settling relatively quickly into the steady-state, as shown in Figure 10(a). For very thin screens ($\delta \rightarrow 0$), this incurred diffraction loss at the end of the line for this case is approximately 14%, which is the lowest value among all four scenarios, and in agreement with Vainstein’s limit (benchmark) [9, 11, 13–15].

B. Nearly matched backed-off Gaussian source

A Gaussian dipole source is also considered, where we align the Gaussian beam’s waist with the first iris, so

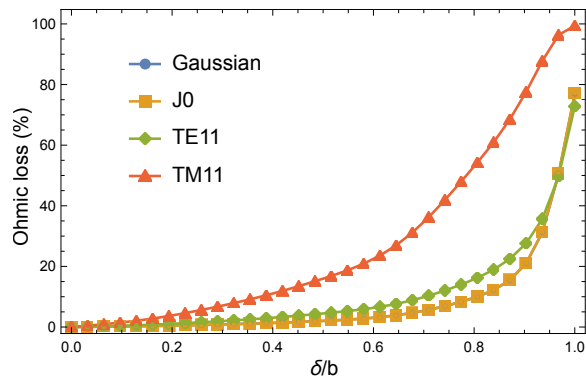


FIG. 12. Behavior of ohmic loss as a function of screen thickness δ , for four types of excitations: $J_0(2.4r/a)$, backed-off Gaussian, TE_{11} , and TM_{11} .

as to have flat wavefronts at this iris's input plane. We control the Gaussian e^{-r^2/w^2} profile by having the $1/e^2$ -width backed off to $\approx 0.65a$. This gives a Gaussian profile of $\exp[-r^2/(0.65a)^2]$ that is better matched to the ideal $J_0(2.4r/a)$ profile [15], for maximum power transfer. The transient regime for this case is shown in Figure 10(b), showing evolution toward the eigenmode that is relatively quick, but not as quick as the $J_0(2.4r/a)$ excitation in Subsection III A. The overall diffraction loss for this case, using thin screens, is approximately 15%, which is slightly higher than the $J_0(2.4r/a)$ excitation case, and in agreement with the forward-scatter theory developed in [15].

C. TE_{11} and TM_{11} sources

Exciting the irisline input with a TE_{11} or TM_{11} source, which are not well matched to the ideal eigenmode, will incur longer transient regimes, as observed in Figures 10(c) and (d), where longer distances are needed for the transient regime to settle down and reach steady-state, especially for TM_{11} . For thin screens, the diffraction loss incurred at the end of the line is approximately 22% for the TE_{11} case, and 54% for the TM_{11} case. This is in agreement with the forward-scatter theory developed in [15].

D. Effect of thicker screens on various modes

By running the analysis for the same structure, $a = 55$ cm, $b = 33.3$ cm, $r_0 = 2a$, and a total line length of 150 m (equivalent to 451 irises) at 3 THz, but with varying screen thickness δ relative to the period b , we can also observe how the ohmic loss and diffraction loss will scale as a function of thickness. This is useful in practice, since thicker screens may be easier for mechanical design and construction. Figures 11 and 12 provide a summary of the behavior of diffraction and ohmic loss

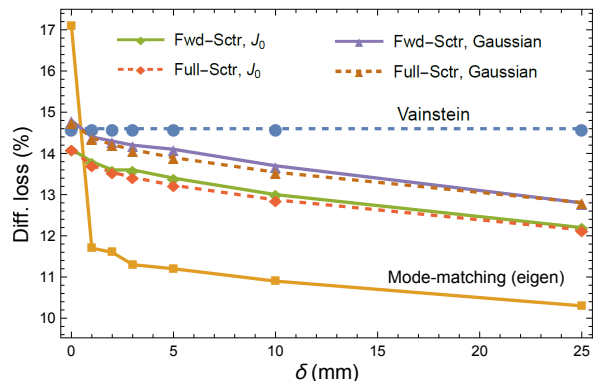


FIG. 13. Comparing predictions from different theories, for the $J_0(2.4r/a)$ and backed-off Gaussian excitations.

as function of δ/b , for the Bessel $J_0(2.4r/a)$, backed-off Gaussian, TE_{11} and TM_{11} modes. We note in these figures how the Gaussian-source case curves tend to closely shadow those of the J_0 -source (they are under each other in Figures 11 and 12). This can be readily explained by noticing the relatively quick settlement of both their transients in Figure 10(a) and (b).

Figure 13 also shown a comparison between the present analysis and the different methods of analysis reported previously, showing good agreement. This includes the Vainstein limit (at $\delta \rightarrow 0$) [9, 11, 13, 14, 22], the mode-matching eigensolution analysis [14], and the forward-scatter field analysis [15]. The results are shown for well matched sources, $J_0(2.4r/a)$ and the backed-off Gaussian. It is seen that the full-scatter and forward-scatter methods are in close agreement with each other in general, validating the use of forward-scatter approximation for such structure, and both agree well with Vainstein's limit for thin screens. The numerical implementation of the mode-matching eigensolution is seen to be in reasonable agreement as well, with approximation 2% deviation from the two scattering theories.

IV. CONCLUSIONS

The full-scatter vector field analysis for an overmoded iris-line structure, with paraxially incident THz radiation pulses, is presented. The spectral (modal) expansion of the full-scatter fields are derived and used to generate the scattering matrices of the waveguide sections. The method is adapted into a computer code and implemented into numerical examples, with different source excitations, showing good agreement with previously established theories, including the Vainstein's limit (benchmark) and the forward-scatter approximation. The results are presented for four difference excitation types: $J_0(2.4r/a)$ Bessel, backed-off Gaussian, TE_{11} , and TM_{11} . Scaling trends for diffraction and ohmic losses are presented, as functions of δ/b , for the four excitation types. This method provides a more accurate analytical frame-

work for estimating the fields in overmoded iris-line structures, as it does not ignore the back-scattered field terms. It also validates the usage of the forward-scatter approximation for analyzing such structures at the high-frequency limit.

ACKNOWLEDGMENTS

The authors would like to thank Nour Elwagdi and Karl Bane for several interesting discussions in relation to

this research. This work was supported by the University of Santa Clara.

Appendix A: Proof and application of Schelkunoff's equivalence theorem

-
- [1] J. D. Jackson, *Classical Electrodynamics*, 3rd ed. (Wiley, 1998).
 - [2] H. Levine and J. Schwinger, On the theory of diffraction by an aperture in an infinite plane screen. i, *Phys. Rev.* **74**, 958 (1948).
 - [3] J. Schwinger and D. Saxon, *Discontinuities in Waveguides: Notes on Lectures by Julian Schwinger*, Documents on modern physics (Gordon and Breach, 1968).
 - [4] R. E. Collin, *Field theory of guided waves*, 2nd ed. (IEEE Press, New York, 1991).
 - [5] A. Zangwill, *Modern Electrodynamics* (Cambridge University Press, 2012).
 - [6] F. E. Borgnis and C. H. Papas, Electromagnetic waveguides and resonators, in *Elektrische Felder und Wellen* (Springer Berlin Heidelberg, Berlin, Heidelberg, 1958) pp. 285–422.
 - [7] D. M. Pozar, *Microwave Engineering* (Wiley, 2011).
 - [8] S. F. Mahmoud, *Electromagnetic Waveguides: theory and applications*, Electromagnetic Waves (Institution of Engineering and Technology, 1991).
 - [9] L. A. Vainstein, *Open Resonators and Open Waveguides* (Colem Press, 1969).
 - [10] J. C. Slater, *Microwave Electronics* (Dover Publishers, 1950).
 - [11] L. A. Vainstein, Open resonators for lasers, *Sov. Phys. JETP* **17**, 709.
 - [12] D. G. Dudley, *Mathematical foundations for electromagnetic theory* (Wiley, 2015).
 - [13] G. Geloni, V. Kocharyan, and E. Saldin, Scheme for generating and transporting thz radiation to the x-ray experimental floor at the lcls baseline (2011), arXiv:1108.1085 [physics.acc-ph].
 - [14] A. Naji, G. Stupakov, Z. Huang, and K. Bane, Field analysis for a highly overmoded iris line with application to thz radiation transport, *Phys. Rev. Accel. Beams* **25**, 043501 (2022).
 - [15] A. Naji and G. Stupakov, Paraxial forward-scatter field analysis for a thz pulse traveling down a highly overmoded iris-line waveguide, *Phys. Rev. Accel. Beams* **25**, 123501 (2022).
 - [16] Z. Zhang, A. S. Fisher, M. C. Hoffmann, B. Jacobson, P. S. Kirchmann, W.-S. Lee, A. Lindenberg, A. Marinelli, E. Nanni, R. Schoenlein, M. Qian, S. Sasaki, J. Xu, and Z. Huang, A high-power, high-repetition-rate THz source for pump-probe experiments at Linac Coherent Light Source II, *Journal of Synchrotron Radiation* **27**, 890 (2020).
 - [17] K. Peetermans, F. Lemery, W. Hillert, W. Decking, K. Floettmann, J. Wernsmann, A. Trebushinin, N. Golubeva, N. Lockmann, B. Steffen, M. K. Czwalianna, M. Dohlus, I. Zagorodnov, J. Richards, F. Giesteira, T. Wohlenberg, L. L. G. Müller, V. Kalendar, D. Thoden, L. Müller, R. Wichmann, S. Walker, M. Guetg, S. Liu, S. Tomin, W. Qin, T. Long, S. Bielawski, M. Krasilnikov, X. Li, G. Geloni, S. Serkez, D. Lipka, A. Novokshonov, G. Kube, I. Hartl, E. Negodin, and M. Scholz, STERN: accelerator-based THz generation at XFEL (Optical Terahertz Science and Technology 2024, Marburg (Germany), 8 Apr 2024 - 12 Apr 2024, 2024).
 - [18] W. Decking, G. Geloni, V. Kocharyan, E. Saldin, and I. Zagorodnov, Scheme for generating and transporting thz radiation to the x-ray experimental hall at the european xfel (2011), arXiv:1112.3511 [physics.acc-ph].
 - [19] S. A. Schelkunoff, Kirchhoof's formula, its vector analogue, and other field equivalence theorems, *Communications on Pure and Applied Mathematics* **4**, 43 (1951), <https://onlinelibrary.wiley.com/doi/pdf/10.1002/cpa.3160040107>.
 - [20] K. Milton and J. Schwinger, *Electromagnetic Radiation: Variational Methods, Waveguides and Accelerators* (Springer, 2006).
 - [21] J. Stratton, *Electromagnetic Theory* (Wiley, 1941).
 - [22] L. Vainshtein, *Electromagnetic Waves* (Radio i svyaz', Moscow, 1988) in Russian.
 - [23] R. Collin, *Foundations for microwave engineering, 2nd ed.*, McGraw-Hill series in electrical engineering: Radar and antennas (Wiley India Pvt. Limited, 2007).